The superficial tufted and mitral cell output neurons of the mouse olfactory bulb have a dual role in insulin sensing

Running Title: Insulin sensing superficial tufted cells

Louis John Kolling[3], Catherine Anne Marcinkiewcz[2] and *Debra Ann Fadool[1,2, 3]

*Corresponding Author
319 Stadium Drive, Suite 3008
King Life Sciences Building
[1]Department of Biological Science
[2]Program in Neuroscience and [3]Institute of Molecular Biophysics
The Florida State University
Tallahassee, FL 32306
USA
dfadool@bio.fsu.edu
850 644-4775

[2]Department of Neuroscience & Pharmacology
The University of Iowa
Iowa City, IA 52242 USA

Number of pages = 48 (including embedded figures and supplemental)
Number of figures = 8
Number of supplementary figures = 1
Number of tables = 2
Supplementary statistical table (excel) = 1

Number of words in manuscript excluding abstract, methods and citations = 5952

KEY WORDS = Kv1.3 channel, insulin, olfactory bulb, tufted cells, output neurons, olfaction

SUMMARY STATEMENT

Superficial tufted cells, as output neurons of the olfactory bulb, were electrophysiologically studied to be insulin sensitive. Brain insulin signaling represents a manner in which olfactory and metabolic circuitry are intertwined.

ABSTRACT

The olfactory bulb (OB) contains multiple, parallel projection neurons to relay the nature of a stimulus. In a mouse *ex vivo* slice preparation, we used patch-clamp electrophysiology to measure intrinsic properties, excitability, action potential (AP) shape, voltage-activated conductances, and neuromodulation in the newly-categorized superficial tufted cells (sTCs) compared with those of mitral cells (MCs). We propose that a marked difference in voltage-dependent current represents distinct ion channel populations that affect the kinetics of action potentials, and evokes an increase in sTC firing frequency, albeit both types of projection neurons having similar AP spiking activity. Triple-colored immunofluorescence and RNA scope were used to detect co-localization of the Kv1.3 ion channel and the insulin receptor in sTCs, with ~73% of sTCs expressing both. The sTCs were modulated by bath application of insulin – increasing AP firing frequency by 97%, attributable to an 8% decrease in the intraburst interval, and a reduction of the latency to first spike by 37%. We conclude that there may be a range of neuromodulators of sTCs that may alter excitability and fine-tune olfactory information processing or metabolic balance.

INTRODUCTION

Sensory systems typically carry multiple types of parallel output, or projection neurons, to relay differing specificity with regards to the nature of the stimulus. The olfactory bulb (OB) processes electrically-encoded odor information, and relays it to overlapping, but not identical, cortical regions via two types of primary projection neurons – namely mitral (MCs) and tufted cells (TCs) (Price and Powell, 1970; Vaaga and Westbrook, 2016). Albeit both receiving synaptic connections from the olfactory sensory neurons (OSNs) at defined and evolutionarily-conserved integration units called glomeruli, less has been studied concerning TCs in terms of biophysical properties and sources of modulation (Liu and Shipley, 2008; Burton and Urban, 2014; Jones et al., 2020). We and other investigators typically recorded from both populations of neurons, referring to them collectively as M/TCs (Fadool and Levitan, 1998; Tucker and Fadool, 2002; Youngstrom and Strowbridge, 2015; Liu et al., 2016). In model organisms, such as drosophila and zebrafish, MCs and TCs are not readily distinguishable from one another (Nagayama et al., 2014). The neurolaminae of mice are significantly more distinct, allowing the complexity of the olfactory circuity to be more easily assessed.

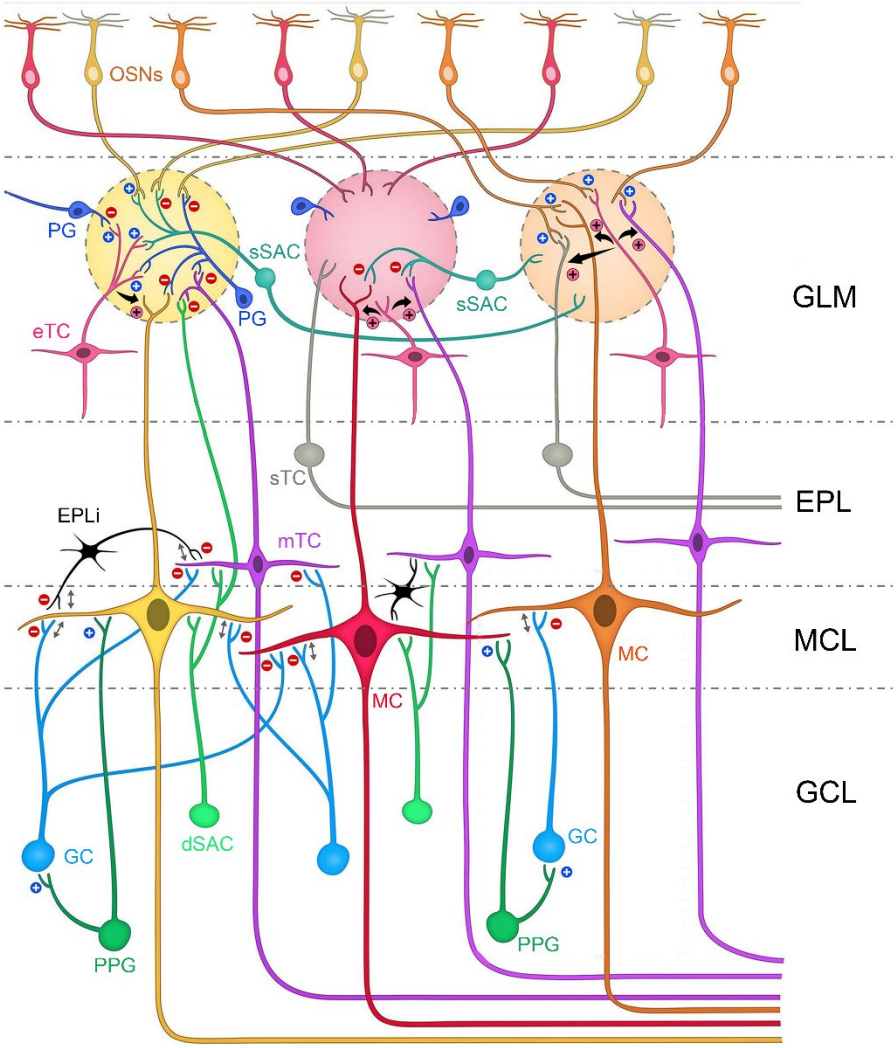

Fig. 1. **Categorization and interactions of the principal projection neurons of the olfactory bulb.** The olfactory bulb neurolamina is divided across the glomerular layer (GLM), external plexiform layer (EPL), the mitral cell layer (MCL), and the innermost granule cell layer (GCL). Also shown is the olfactory mucosa containing the olfactory sensory neurons (OSNs). This schematic highlights the four classes of output or projection neurons, namely the external tufted cells (eTCs, pink), the superficial tufted cells (sTCs, gray), the middle tufted cells (mTCs, purple), and the mitral cells (MCs, red). The soma of the eTCs are found within the GLM. The sTC soma reside in the superficial one-third of the EPL. The deep two-thirds of the EPL contain both the mTCs and misplaced MCs. The MCL houses the eponymous MCs. Blue plus signs (+) represent excitatory synapses, red minus signs (-) represent inhibitory synapses, and pink plus signs (+) represent excitatory dendro-dendritic interactions originating from external tufted cells (eTCs). Reciprocal synapses are denoted by a double arrow. PG = periglomerular cell, sSAC = superficial short axon cell, EPLi = interneuron of the external plexiform layer, GCL = granule cell layer, GC = granule cell, PPG = preproglucagon neuron, dSAC = deep short axon cell. *Modified from Huang* et al. *2021.*

101 Like many budding areas of research, the standardization of categorical terminology is not
102 considered until there is enough information to classify. Jones et al. 2020 aptly stated that the
103 *"nomenclature around TC subtypes has been somewhat confusing in the field* (Jones et al.,
104 2020)." Both early works and more recent reviews describe 4 distinct classes of projection
105 neurons – external TC, internal TC, middle TC, and MC (Pinching and Powell, 1971a,b;
106 Mori, 1987; Shepherd, 2004; Hayar et al., 2004; Mori and Sakano, 2022). A more recent
107 work proposed to alternatively reclassify output neurons based upon size and location into
108 three types: putative MCs (pMC; >20 um diameter and located in the MCL), EPL located TC
109 (lower EPL TC; <20 um diameter), and putative TC (pTC; <20 um diameter located in the
110 MCL) (Gadiwalla et al., 2025). Herein, our study uses the naming convention originating
111 from Cajal and then reestablished by Jones et al. (2020), based upon the position of the TC
112 soma within its respective neurolamina – namely, external tufted cells (eTCs), middle tufted
113 cells (mTCs), and superficial tufted cells (sTCs) (**Fig. 1**). Of the three subclasses of TCs, the
114 eTC are the best studied. The eTCs are a select population of juxtaglomerular cells that
115 demonstrate rhythmic and spontaneous action potential bursting (Hayar et al., 2004a,b, 2005;
116 Antal et al., 2006; Zhou et al., 2006; Ma and Lowe, 2007; Liu and Shipley, 2008). The eTC
117 are known to receive monosynaptic input from olfactory sensory neurons (OSNs) and
118 establish glutaminergic synaptic connections to short-axon cells and periglomerular cells
119 within the bulb (Hayar et al., 2004a,b, 2005), and their activation can provide feedforward
120 excitation of MC (De Saint Jan et al. 2009). eTCs actually process sensory input before it
121 reaches the sTCs and MCs (De Saint Jan et al., 2009; Najac et al., 2011; Gire et al., 2012;
122 Igarashi et al., 2012; Vaaga and Westbrook, 2016). The eTCs receive the greatest signal from
123 activated OSNs, and stimulate neighboring sTCs, mTCs, and MCs via glutamatergic dendro-
124 dendritic interactions (De Saint Jan *et al*., 2009; Najac *et al*., 2011; Jones *et al*., 2020). This
125 feed-forward excitation from eTCs provides "biphasic input" to other M/TCs that may also
126 receive direct monosynaptic input from a specific OSN family member (Najac *et al*., 2011;
127 Vaaga and Westbrook, 2016; Jones *et al*., 2020).
128
129 Because the eTC are well characterized, and the mTCs are less accessible for patch-clamp
130 recordings, we decided to focus our study on a lesser known type of TC, the sTC, which are
131 expressed superficially in the external plexiform layer (EPL)(Jones et al., 2020; Chen et al.,

132 2024). mTC soma are found between the MCL and the inner (deep) two-thirds of the external
133 plexiform layer (EPL), whereas the soma of superficial tufted cells (sTCs) are located in the
134 outer (superficial) one-third of the EPL. Like MCs, sTCs and mTCs receive input from
135 olfactory sensory neurons (OSNs) at defined glomeruli, and pass sensory information to
136 various subcortical areas. The sTCs and mTCs, however, project, to distinctly different brain
137 regions than MCs; even if a M/TC pair projects to the same subcortical region, it will project
138 to different parts of it (Nagayama et al., 2010, 2014; Igarashi et al., 2012). Excellent
139 foundational work has been done to characterize the innate biophysical differences between
140 TCs and MCs (Burton and Urban, 2014), but the categorization of the assessed cells preceded
141 the boundaries set by the current naming methods (Jones et al., 2020). As such, no previous
142 report has characterized the innate biophysical differences between MCs and sTCs, nor
143 investigated the function of sTCs to sense metabolically-relevant molecules or
144 neuromodulators.
145
146 In this study, we compare the biophysical properties of MCs and sTCs in *ex vivo* brain slices
147 from male and female mice. Using current- and voltage-clamp recordings, we found that
148 action potential (AP) properties and voltage-activated currents differed between sTCs and
149 MCs. To better understand the complementary function of sTCs to MCs, we examined the
150 response of sTCs to a known modulator and a vestibule blocker of Kv1.3 – a predominant ion
151 channel carrying 60-80% of the outward current in MCs (Fadool and Levitan, 1998; Colley et
152 al., 2004). Our results directly show that sTCs are more excitable than MCs. This is correlated
153 with differing voltage-activated currents, and a differing AP shape. We further find that sTCs
154 are modulated by the presence of insulin, suggesting a role for sTCs in metabolic circuitry
155 (Fadool et al., 2004; Palouzier-Paulignan et al., 2012; Aimé et al., 2014). Our study
156 demonstrates that the Kv1.3 ion channel is necessary for the insulin-sensing property of sTCs,
157 as it is in MCs (Fadool et al., 2004, 2011; Tucker et al., 2013).
158

159 ## RESULTS

160 **Superficial tufted cells have greater input resistance and slightly lower voltage-**
161 **activated current at hyperpolarizing potentials than that of mitral cells**

162 Superficial tufted cells (sTCs) have greater EPSC amplitude when stimulated by direct
163 olfactory sensory neuron activation over that of mitral cells (MCs) (Jones et al., 2020), albeit
164 both being the predominant output neurons of the OB. Less has been studied to reveal the
165 nature of intrinsic properties and voltage-activated conductances in sTCs. We used ex vivo
166 slice electrophysiology in the voltage-clamp configuration, therefore, to study intrinsic
167 properties as well as outward currents, which are largely driven by the Kv1.3 channel in MCs
168 (Fadool *et al*., 1997; Fadool and Levitan, 1998). The resting membrane potential (RMP) was
169 not significantly different between MCs and sTCs (MCs = -55.8 $\pm$ 6.3 mV (20) vs. sTCs = -
170 58.0 $\pm$ 6.5 mV (22); Student's *t*-test, p = 0.2906).
171
172 Macroscopic currents were acquired in response to a series of 400 ms duration (P_d) voltage
173 steps that increased in increments of 20 mV from -100 mV to +40 mV. The resulting current-
174 voltage (IV) relationship was plotted in **Fig. 2A** using the peak transient current value for each
175 step normalized to the +40 mV step. It was noted that the amplitude of the outward current at
176 hyperpolarizing potentials (a window between -60 to -20 mV) was significantly greater in
177 MCs vs. that of TCs (**Fig. 2B**). A two-way repeated measure, mixed factor analysis of
178 variance (2-w RM mixed ANOVA) was applied using cell type and voltage as factors. There
179 was a main effect of cell type (F (1, 22) = 9.430; p = **0.0056) as well as a voltage x cell type
180 interaction (F (7, 154) = 5.542; p <0.0001). A Sidak's post-hoc test showed that the evoked
181 current was significantly greater for MCs at the -60 mV (p = 0.0202), -40 mV (p = 0.0049)
182 and -20 mV (p = 0.0311) voltage steps. This difference only existed in this hyperpolarized
183 window and was not observed once highly depolarized at the +40 mV step (**Fig. 2C**, MCs =
184 5180 $\pm$ 2540 pA (11) vs. sTCs = 3746 $\pm$ 1030 pA (13), Mann-Whitney U, p = 0.2066). We
185 next measured the kinetics of inactivation and deactivation for the voltage-activated currents
186 at a hyperpolarized (V_c = -40 mV) and depolarized (V_c = +40 mV) range, respectively. The
187 kinetics of inactivation (τ_{Inact}) did not differ between cell types (**Fig. 2D, Left**, MCs = 71.2 $\pm$
188 19.0 ms (10) vs. sTCs = 57.0 $\pm$ 28.6 ms (13), Student's *t*-test, p = 0.1894) at V_c = -40 mV,
189 however the kinetics of deactivation (τ_{Deact}) was significantly faster for sTCs at this command
190 voltage (**Fig. 2D, Right**, MCs = 2.19 $\pm$ 0.67 ms (11) vs. sTCs = 1.47 $\pm$ 0.61 ms (13), Mann-
191 Whitney U, *p = 0.0107). Neither time constant differed between cell types at a V_c = +40 mV
192 step (**Fig. 2E**, τ_{Inact}: MCs = 75.6 $\pm$ 30.9 ms (11) vs. sTCs = 158 $\pm$ 140 ms (13), Mann-Whitney

193 U, $p = 0.3031$; τ_{Deact}: MCs = 1.14 ± 0.41 ms (10) vs. sTCs = 1.12 ± 0.52 ms (13), Student's *t*-
194 test, $p = 0.9043$). Overall, although sTCs tend to have higher input resistance than MCs, the
195 outward voltage-activated currents of sTCs are less responsive to changes in voltage.

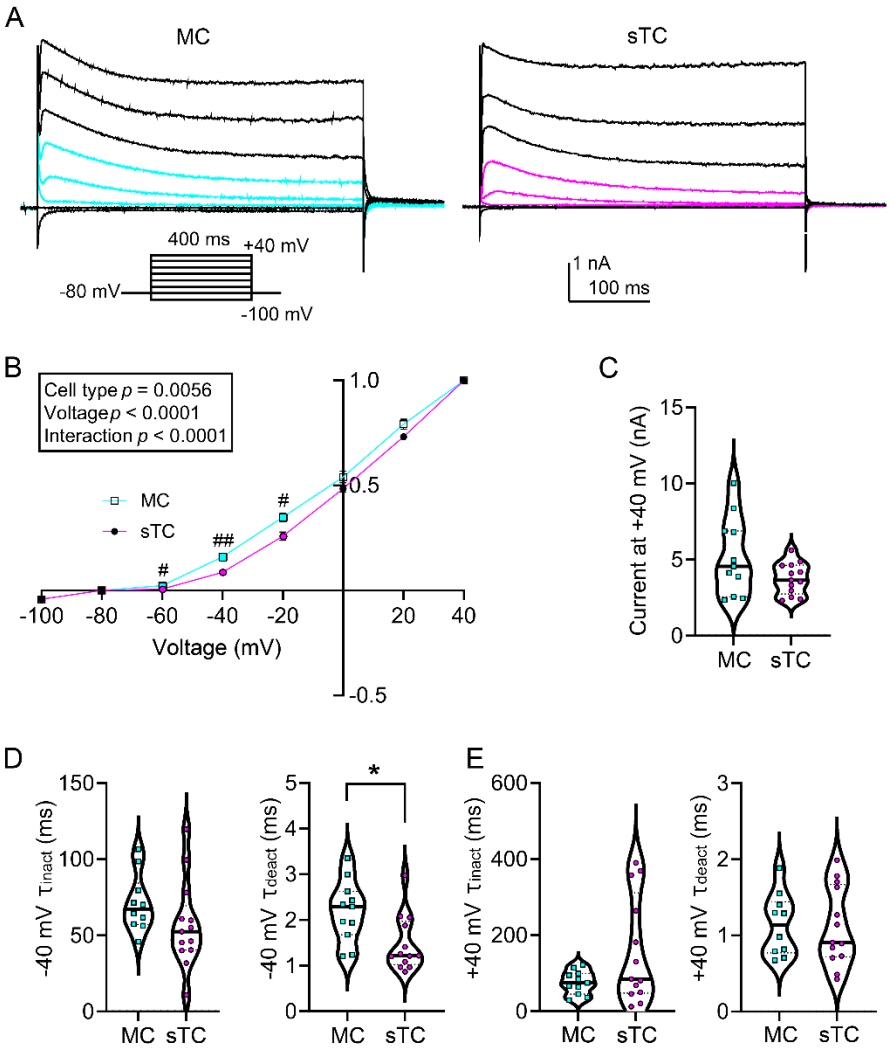

196 **Fig. 2.** Outward voltage-activated current properties of mitral cells and superficial tufted cells. ***A,***
197 Family of voltage-activated currents, V_h = -80 mV where V_c was stepped in 20 mV increments from -
198 100 mV to +40 mV using a P_d = 400 ms. Colored sweeps correspond to significantly different
199 colored data points in (***B***). ***B,*** Normalized IV plots (2-w mixed RM ANOVA, cell type ***p =
200 0.0056, Sidak's post-hoc test, $^{\#}p < 0.05$, $^{\#\#}p < 0.01$; voltage x cell type interaction ****$p < 0.0001$).
201 ***C,*** Violin plot of non-normalized peak transient voltage-activated current at +40 mV, Mann-Whitney
202 U. Violin plot of the *Tau* of inactivation (*left*) and deactivation (*right*) at **(D)** Vc = -40 mV and **(E)**
203 +40 mV, respectively, Mann-Whitney U (*p = 0.0107). MC = mitral cell population sampled, sTC =
204 superficial tufted cell population sampled.

205 **Kv1.2 and Kv1.3 expression is similar between superficial tufted and mitral**
206 **cells**

207 The drug MgTx is a selective blocker of Kv1.2 and Kv1.3 ion channels when applied to the
208 extracellular membrane at 1 nM concentration (Garcia-Calvo et al., 1993; Garcia et al., 1997;
209 Bartok et al., 2014). It has a slow k_{on} of 10 min and an even slower k_{off} of 2 h (Garcia-Calvo et
210 al., 1993; Nikouee et al., 2012; Chen and Chung, 2014), therefore, we did not attempt a
211 washout of the vestibule blocker during our patch recording. After collecting baseline voltage-
212 clamp recordings on MCs for 15 min, 1 nM MgTx was added to the bath to wash over the
213 slice for 15 min. Another set of voltage-clamp recordings was then collected (**Fig. 3A**). The
214 same repeated-measure paradigm was then applied to a separate group of sTCs (**Fig. 3B**).
215 MgTx reduced voltage-activated currents in both MCs and sTCs in a voltage-dependent
216 manner (**Fig. 3C).** Here, a 2-w mixed RM ANOVA was applied using drug and voltage as
217 factors. For the MC recordings, there was a main effect of drug ($F(1, 9) = 43.62$, ****$p <$
218 0.0001) as well as a voltage x drug interaction ($F(7, 63) = 43.86$, ****$p < 0.0001$). A Sidak's
219 post-hoc test demonstrated significant differences at the -20 mv ($^{\#\#\#}p = 0.0008$) voltage step
220 and all further depolarizing steps ($^{\#\#\#\#}p < 0.0001$). For the sTC recordings, there was a main
221 effect of drug ($F(1, 12) = 25.51$, ***$p = 0.0003$) as well as a voltage x drug interaction ($F(7,$
222 $60) = 19.87$, ****$p < 0.0001$). A Sidak's post-hoc test demonstrated significant differences at
223 -30 mv and above ($^{\#\#\#\#}p < 0.0001$). Using a 3-way mixed-effects analysis (3-w mixed RM
224 ANOVA), we found no difference in MgTx-mediated effects on voltage dependence between
225 MCs and sTCs (**Fig. 3C, Bottom**, voltage x cell type x drug interaction $F(7, 123) = 0.7633$, p
226 $= 0.6190$).
227
228
229
230
231
232
233
234

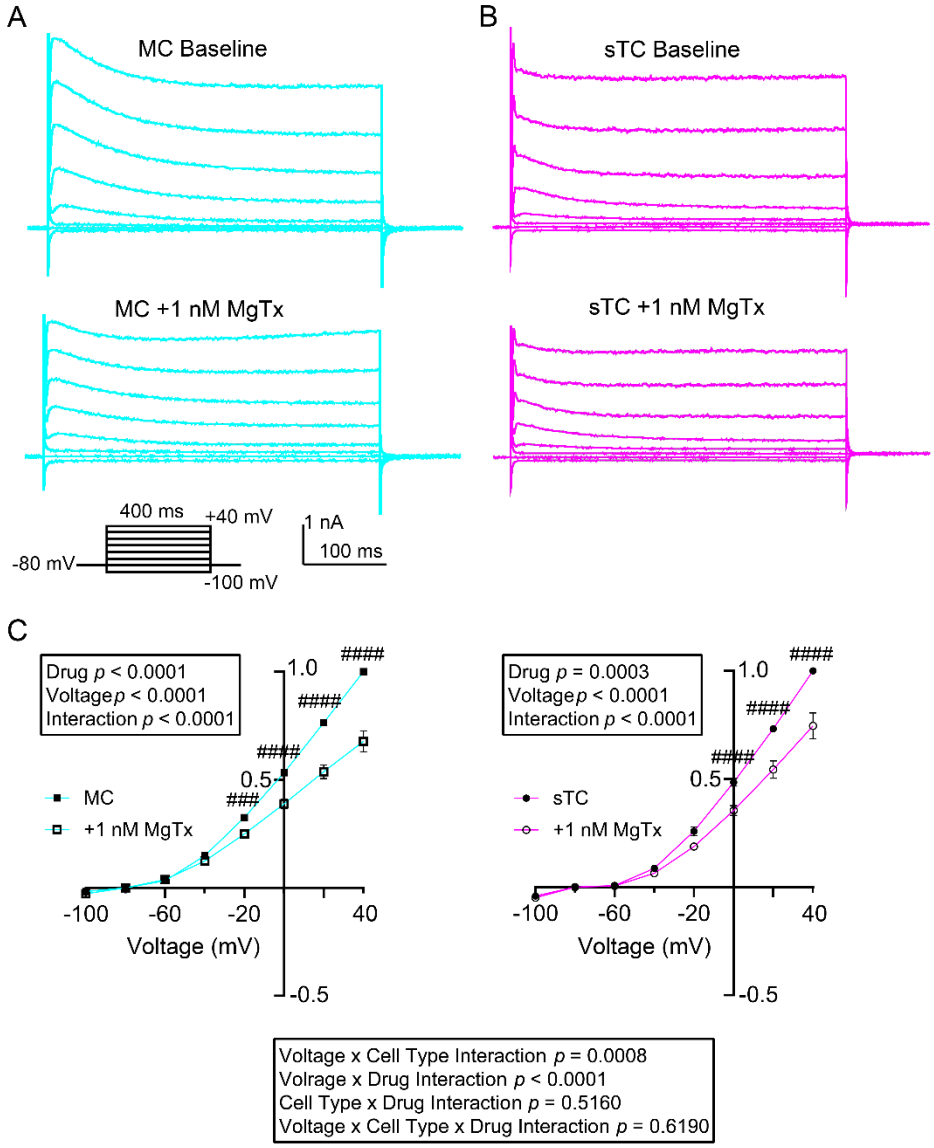

Fig. 3. Sensitivity of mitral and superficial tufted cells to a selective blocker of Kv channels. ***A,*** Family of voltage-activated currents recorded as in Figure 3 prior (***Top,*** Baseline) and following (***Bottom,*** +1 nM MgTx) 15-min bath application of margatoxin (MgTx) in a representative ***A,*** mitral cell (MC) and ***B,*** superficial tufted cell (sTC). ***C,*** Normalized IV plots prior (solid symbols) and following (open symbols) bath application of MgTx in a population of MCs (***Left,*** 2-w mixed RM ANOVA, drug F (1, 9) = 43.62, ****$p < 0.0001$, with a Sidak's post hoc test, $^{\#\#\#}p = 0.0008$, $^{\#\#\#\#}p < 0.0001$; voltage x drug interaction F (7, 63) = 43.86, ****$p < 0.0001$) and a population of sTCs (***Right,*** 2-w mixed RM ANOVA, drug ***$p = 0.0003$, Sidak's post-hoc test, $^{\#\#\#\#}p < 0.0001$; voltage x drug interaction ****$p < 0.0001$). ***C, Bottom*** – 3-way mixed RM ANOVA result comparing the two IV plots in ***C, Left-Right*** (3-w mixed RM ANOVA, voltage x cell type interaction F (7, 123) = 3.879, ***$p = 0.0008$; voltage x drug interaction F (7, 123) = 57.42, ****$p < 0.0001$; cell type x drug interaction F (1, 123) = 0.4244, $p = 0.5160$; voltage x cell type x drug interaction F (7, 123) = 0.7633, $p = 0.6190$).

248 **Superficial tufted cells are more excitable than mitral cells**

249 We next wanted to compare evoked AP firing frequency between MCs and sTCs as a metric
250 for cellular excitability. After obtaining the whole-cell configuration, cells were current-
251 clamped using a V_h of -60 mV (near RMP) for comparison of excitability across cell types.
252 Each MC or sTC was stimulated with a family of injected current steps that increased in 25
253 pA increments from -50 pA to 175 pA (**Fig. 4A**) to determine the threshold for first firing. On
254 average, the current needed to evoke APs (rheobase) was lower in sTCs than in MCs (**Fig. 4B**,
255 MCs = 69.3 $\pm$ 44.9 pA (22) vs. sTCs = 34.2 $\pm$ 24.1 pA (30), Mann-Whitney U, $^{**}p = 0.0021$).
256 Both cell types increased AP firing frequency in response to current step, but sTCs had a
257 significantly greater frequency than that of MCs (**Fig. 4C**). Here, we applied a 2-w mixed RM
258 ANOVA using cell type and current as factors. As anticipated, there was a main effect for
259 injected current ($F(7, 263) = 71.39$, $^{****}p < 0.0001$). There was also a main effect for cell
260 type ($F(1, 51) = 11.92$, $^{**}p = 0.0011$) and a current x cell type interaction ($F(7, 263) = 3.656$,
261 $^{***}p = 0.0009$). A Sidak's post-hoc test indicated a significant difference in current
262 dependence at the current injection window between 25 and 75 pA (25 pA - $^{\$\$}p = 0.0077$, 50
263 pA - $^{\$\$}p = 0.0017$, and 75 pA - $^{\$\$\$}p = 0.0001$). The increased AP firing frequency in response
264 to injected current was likely attributed to a change in interspike interval (ISI). As shown in
265 **Fig. 4D**, the ISI was shorter in sTCs compared to that of MCs. A 2-w mixed RM ANOVA
266 using cell type and injected current as factors demonstrated a main (negative) effect for
267 injected current ($F(1.643, 38.07) = 33.74$). There was also a main effect for cell type ($F(1,$
268 $49) = 37.53$, $^{****}p < 0.0001$) and a current x cell type interaction ($F(6, 139) = 5.873$, $^{****}p$
269 < 0.0001). A Sidak's post-hoc test indicated a significant difference between cell types at the
270 current injection window between 100 and 150 pA (100 pA - $^{\#}p = 0.0101$, 125 pA - $^{\#\#}p$
271 $= 0.0022$, and 150 pA - $^{\#}p = 0.0294$).
272
273
274
275
276
277

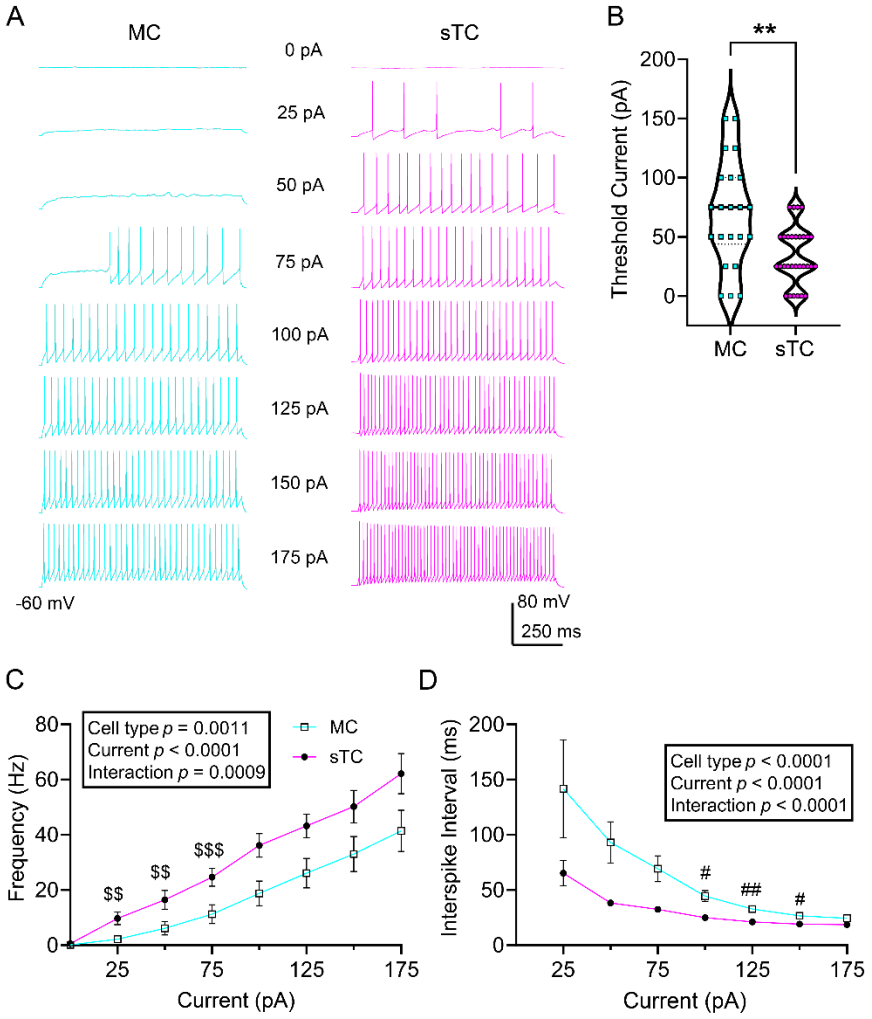

Fig. 4. Spike firing properties compared between mitral cells (MC) and superficial tufted cells (sTC). ***A*,** Representative action potential trains evoked by various current steps as indicated, recorded from a MC (***Left***) vs. sTC (***Right***). ***B*,** Violin plot comparing the current needed to evoke action potentials (rheobase), Mann-Whitney U, $^{**}p = 0.0021$. Line plots for ***C*,** mean spike frequency across current step and ***D*,** mean interspike interval (ISI). Line plot data were analyzed with a ***(C)*** 2-w mixed RM ANOVA, cell type $^{**}p = 0.0011$; current x cell type interaction $^{***}p = 0.0009$, Sidak's post-hoc test, $^{\$\$}p < 0.01$, $^{\$\$\$}p < 0.001$, ***(D)*** 2-w mixed RM ANOVA, cell type $^{****}p < 0.0001$; current x cell type interaction $^{****}p < 0.0001$, Sidak's post-hoc test, $^{\#}p < 0.05$, $^{\#\#}p < 0.01$.

Because potassium channel currents can greatly influence the characteristics of APs (**Fig. 2-4**), we wanted to determine any differences in AP shape or kinetics that could accompany these findings. Many AP parameters require a clearly defined baseline in order to be assessed accurately, and the parameters are dependent on current injection magnitude. The metrics of

291 ‘maximum decay slope’ and ‘time to achieve maximum decay slope’ are not dependent upon
292 correct identification of the recording baseline, and we therefore examined these metrics
293 simultaneously across all current injection steps. sTCs achieved steeper maximum decay
294 slopes than MCs, which also differed in a current-dependent manner (**Fig. 5A, C**). We applied
295 a 2-w mixed RM ANOVA using cell type and current step as factors. There was a main effect
296 of cell type (F (1, 50) = 5.914, $^{*}p = 0.0186$) and a current x cell type interaction (F (6, 127) =
297 5.562, $^{****}p < 0.0001$); a Sidak’s post-hoc test indicated that cell-type significant differences
298 occurred at current steps 50 pA - $p^{\#\#\#} = 0.0006$, 75 pA - $^{\#\#\#\#}p < 0.0001$, and 100 pA - $^{\#\#}p =$
299 0.0074. APs recorded in sTCs also exhibited faster times to achieve maximum decay slope
300 than those in MCs, independent of current injection step (**Fig. 5B, C**). We applied a 2-w
301 mixed RM ANOVA using cell type and current step as factors. There was no effect of current
302 step (F (0.1425, 3.016) = 9.085, $p = 0.0524$), but there was a main effect of cell type F (1, 50)
303 = 4.088, $^{*}p = 0.0486$. A Sidak’s post-hoc test, demonstrated that sTCs were faster at all
304 current injections at and above 75 pA (75 pA - $^{\#\#\#}p = 0.0002$, 100 pA - $^{\#\#}p = 0.0031$, 125 pA -
305 $^{\#}p = 0.0300$, 150 pA - $^{\#}p = 0.0274$).
306
307 Due to differences in excitability between MCs and sTCs (**Fig. 4**), the current injection step of
308 75 pA had the largest sample size for the comparison of AP characteristics that are dependent
309 upon verifiable baseline. Overall, we found that the APs of sTCs have greater peak
310 magnitude, greater antipeak (after-hyperpolarization) amplitude, faster rise kinetics, and faster
311 decay kinetics than MCs (**Table 1**). Mean values, sample sizes, *p* values, and statistical tests
312 are reported within each column.
313

	Peak Amplitude (mV)	Time to Peak Amplitude (ms)	Antipeak Amplitude (mV)	Time to Antipeak (ms)	Half Width (FWHM) (ms)
Mitral Cells	51.1 ± 10.0	5.83 ± 0.26	-12.1 ± 2.4	11.4 ± 0.7	1.78 ± 0.36
N	11	11	11	11	11
Superficial Tufted Cells	60.8 ± 7.0	5.72 ± 0.09	-15.1 ± 2.5	9.20 ± 0.90	1.32 ± 0.16
N	11	11	11	11	11
p-value	**0.0150**	ns (0.1970)	**0.0079**	**< 0.0001**	**< 0.0001**
Test used	†	†	⊤	†	⊤

	Max Rise Slope (mV/ms)	Time to Max Rise Slope (ms)	Max Decay Slope (mV/ms)	Time to Max Decay Slope (ms)	Rise Time to Half Amplitude (ms)
Mitral Cells	88.4 ± 35.2	5.11 ± 0.17	-44.3 ± 13.2	0.866 ± 0.167	5.09 ± 0.11
n	15	11	15	15	11
Superficial Tufted Cells	117.0 ± 44.0	5.06 ± 0.17	-79.5 ± 20.4	0.612 ± 0.105	5.11 ± 0.05
n	20	11	20	20	11
p-value	**0.0493**	ns (0.8338)	**< 0.0001**	**< 0.0001**	ns (0.7969)
Test used	†	⊤	‡	†	⊤

	Decay Time to Half Amplitude (ms)	Rise Slope 10% to 90% (mV/ms)	Rise Time 10% to 90% (ms)	Decay Slope 90% to 10% (mV/ms)	Decay Time 90% to 10% (ms)
Mitral Cells	6.87 ± 0.38	58.8 ± 24.1	1.04 ± 0.82	-31.3 ± 8.2	1.41 ± 0.21
n	11	11	11	11	11
Superficial Tufted Cells	6.43 ± 0.16	74.1 ± 18.3	0.784 ± 0.151	-56.7 ± 11.2	0.911 ± 0.107
n	11	11	11	11	11
p-value	**0.0021**	ns (0.1087)	ns (0.3192)	**< 0.0001**	**< 0.0001**
Test used	†	‡	†	‡	†

314 **Table 1.** Action potential shape compared between mitral cells (MCs) vs. superficial tufted cells
315 (sTCs). Recordings were made while holding cells near rest (V_h = -60 mV) and injecting 75 pA of
316 current. Values are mean ± standard deviation. ns = not significant, †= Student's *t*-test, ‡= *t*-test with
317 Welch's correction, ₸= Mann-Whitney U.

318

319 **Superficial tufted cells do not show a higher propensity to bursting activity**
320 **than mitral cells**

321 Previous reports demonstrate that MCs are less likely to exhibit trains of AP activity than TCs
322 in general (Liu and Shipley, 2008; Burton and Urban, 2014; Jones *et al*., 2020). As such, we
323 wanted to determine if this was also true of sTCs by applying further refined spike analysis.
324 After determining the supra-threshold current injection step, we injected cells at that threshold
325 using a P_d of 5000 ms and a T_s = 30 s for 10 total sweeps (**Fig. 5D**). We defined a "train" as
326 having 3 or more APs within a 100 ms period (Balu et al., 2004), and only directly compared
327 cells receiving identical current injection magnitude. sTCs did not exhibit more AP trains
328 within their respective recording periods (**Fig. 5E,** MCs = 28.7 ± 21.1 (7) AP trains vs. sTCs =
329 25.1 ± 21.3 AP trains (7), Student's *t*-test, p = 0.7582), nor did the trains of sTCs contain more
330 AP spikes (**Fig. 5F,** MCs = 10.8 ± 11.9 spikes/train (6) vs. sTCs = 11.3 ± 7.2 spikes/train (6),
331 Student's *t*-test, p = 0.2796). sTCs did not exhibit differing pause duration between trains
332 (**Fig. 5G,** MCs = 950 ± 890 ms (6) vs. sTCs = 1660 ± 1720 ms (6), Mann-Whitney U, p =
333 0.3939), nor a differing latency period to first spike (**Fig. 5H,** MCs = 327 ± 249 ms (6) vs.
334 sTCs = 535 ± 404 ms (7), Mann-Whitney U, p = 0.1375). To assess whether sTCs showed a
335 higher propensity to be a 'bursting cell' (as opposed to a regularly-firing cell), we assessed the
336 firing activity from all current-clamp recordings to determine the categorical type of each MC
337 and sTC. A cell was categorized as a "bursting cell" if any of its sweeps contained at least two
338 bursts separated by a pause duration of > 100 ms. sTCs did not show a statistically different
339 preference toward bursting or regularly firing than that of MCs (**Fig. 5I**, MCs = 28.6% (21),
340 sTCs = 40% (30), Chi-squared test, p = 0.40061, X^2 = 0.7065).

341

342

343

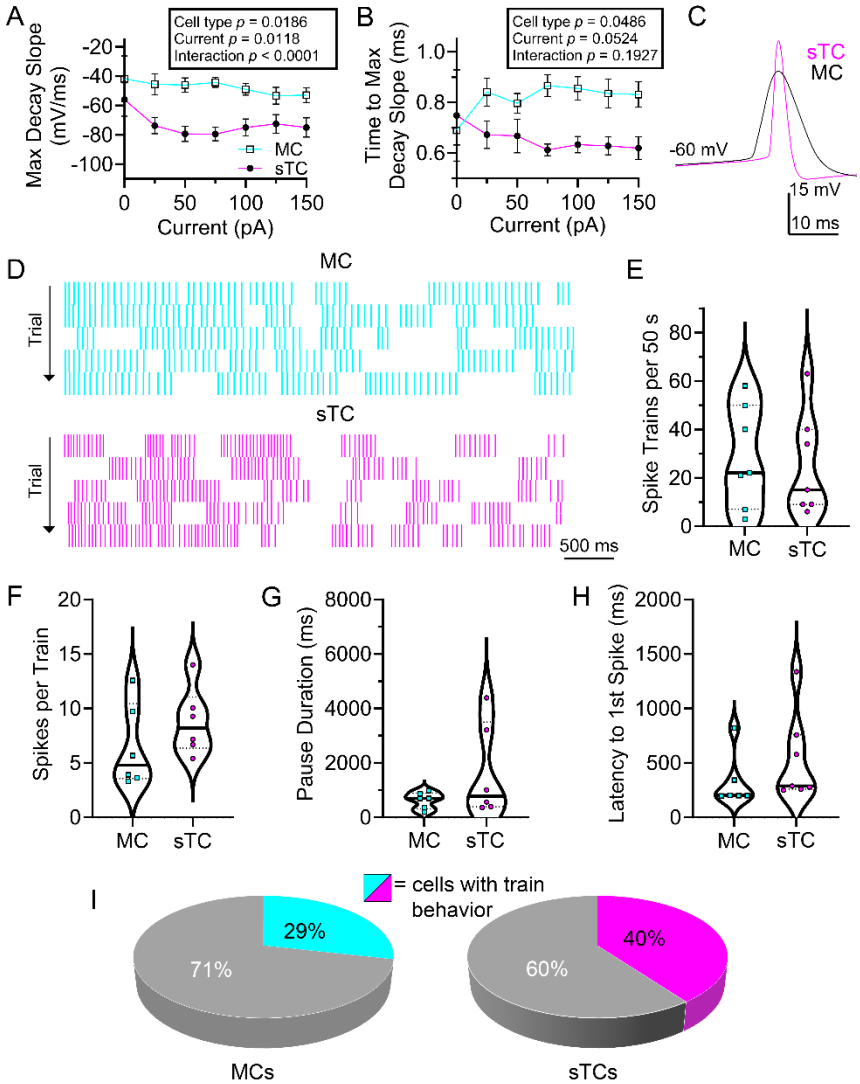

Fig. 5. Action potential shape and spike train activity compared between mitral cells (MC) and superficial tufted cells (sTC). Line plot for ***A,*** maximum decay slope (max decay slope) and ***B,*** time to achieve maximum decay slope from peak magnitude (time to max decay slope) across current step. Line plot data were analyzed with **(A),** 2-w mixed RM ANOVA, cell type *p = 0.0186, Sidak's post-hoc test, ##p < 0.01, ###p < 0.001; current x cell type interaction ****p < 0.0001, **(B),** 2-w mixed RM ANOVA, cell type *p = 0.0486, Sidak's post-hoc test, #p < 0.05, ##p < 0.01, ###p < 0.001. ***C,*** Representative pair of action potentials recorded in response to a 75 pA current injection held near rest (Vh = -60 mV). ***D,*** Representative raster plot for a cell stimulated with a 50-pA current injection using a P_d = 5 s for each cell type, respectively. Successive trials are stacked vertically below. Violin plots computed across a 50 s recording period (10, 5s sweeps) compare ***E,*** mean number of bursts, ***F,*** mean spikes per train, ***G,*** mean pause duration between trains, and ***E,*** mean latency to first spike. ***E-F,*** were analyzed using a Student's *t*-test, ***G-H*** were analyzed using Mann-Whitney U; $p > 0.05$. ***I,*** Relative proportion of cells eliciting spike train behavior among sampled MCs (***Left***) and sTCs (***Right***), respectively (Chi-squared test, p = .40061, $X^2 = 0.7065$, n = 51).

359 **Co-localization of Kv1.3 channel and the insulin receptor in superficial tufted**
360 **cells**
361
362 MCs are known be modulated by insulin, and Kv1.3 is necessary for this modulation (Fadool
363 and Levitan, 1998; Fadool et al., 2000, 2011; Tucker et al., 2010; Kuczewski et al., 2014). We
364 found sTCs to be modulated by margatoxin (**Figure 3**), suggesting expression of Kv1.3. We
365 therefore performed multiplex fluorescent *in situ* hybridization (RNAscope) to determine co-
366 expression of Kv1.3 and the insulin receptor (IR) in sTCs, similar to what we have observed
367 for MCs (Marks and Fadool, 2007; Colley et al., 2009; Marks et al., 2009; Thiebaud et al.,
368 2016). Using a transgenic GFP label for M/TCs under control of the *Tbx21* promoter, we
369 performed RNAscope targeting *Kv1.3*, *GFP*, and *Insr* on six coronal sections sampled 512 µm
370 apart along the antero-posterior axis (AP axis), in both male and female mice. We observed
371 co-localization of the channel and the receptor markedly distributed with the expression of the
372 *Tbx21* promoter by imaging at low power across the entire olfactory bulb (**Fig 6A-D**). We
373 then moved to higher magnification in the EPL to visualize the sTC specifically, and the
374 colocalization of the channel and receptor with the *Tbx21* reporter expression (**Fig. 6E-H**). A
375 2-way comparison revealed a main effect of AP axis on Tbx21+ cell count (**Fig. 6I**, **p* =
376 0.0118) with no interactive effect of axis on sex or laminar layer (*p* = 0.3020; M MCL, M
377 EPL, M GLM, F MCL, F EPL, F GLM as columns variables; M = male, F = female). We then
378 examined the percentage of Tbx21+ cells co-labeled with both *Kv1.3* and *Insr* along the
379 antero-posterior axis, and found no main effect of AP axis (**Fig. 6J,** *p* = 0.5736) or interactive
380 effects on sex or laminar layer (*p* = 0.7359). Without regard for antero-posterior position or
381 sex (since these were not found to be factors for co-labeling), we assessed the percentage of
382 Tbx21+ cells that express both *Kv1.3* and *Insr*. We find triple-labeling of 82.1 ± 4.3 % in the
383 MCL, 73.4 ± 8.2 % in the EPL, and 76.2 ± 6.8 % in the GLM. ANOVA comparisons across
384 neurolaminae revealed a subtle difference in the percentage of all Tbx21+ cells expressing
385 *Kv1.3* alone (**Fig. 6K**, **p* = 0.0159) and expressing both *Kv1.3* and *Insr* (**Fig. 6M**, **p* =
386 0.0373). We further performed immunolabeling for Kv1.3 and Insr proteins in tandem with
387 Tbx21 reporter expression. As predicted based upon previous reports (Marks *et al*., 2009;
388 Colley *et al*., 2009), co-labeling for both IR and Kv1.3 was observed in the soma and near the
389 axon initial segment of most MCs imaged (**Fig. S1**).

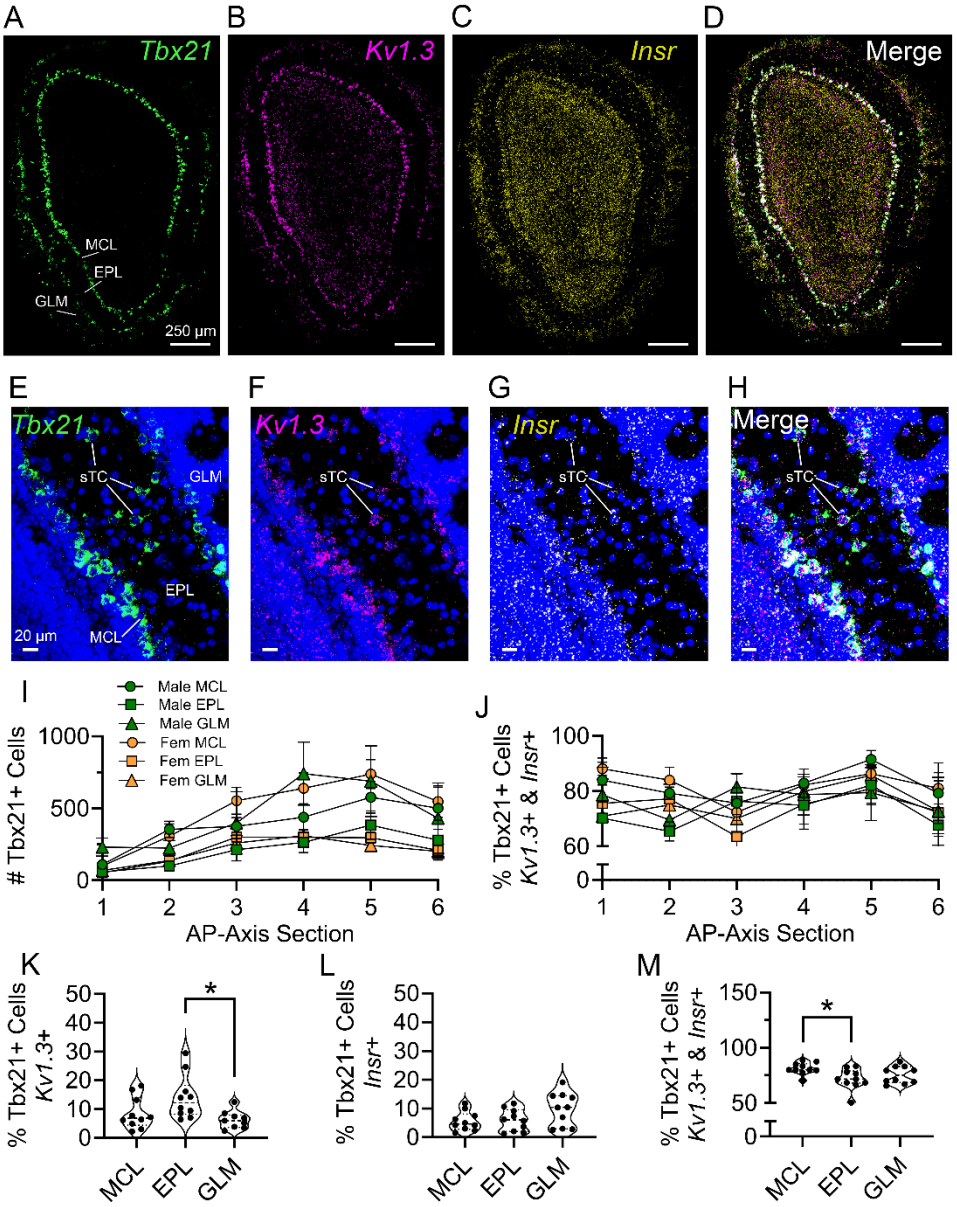

Fig. 6. Colocalization of M/TCs with the Kv1.3 channel (*Kv1.3*) and insulin receptor (*Insr*) using RNAscope. Photomicrographs demonstrating neurolaminar distribution of Tbx21 reporter expression (green, ***A***), *Kv1.3* expression (magenta, ***B***), and *Insr* expression (yellow, ***C***), separately and merged (white, ***D***). ***E–H***: Same as ***A–D***, but to demonstrate localization to sTCs with the inclusion of a DAPI nuclear stain. ***I:*** Coronal sections were sampled along the anter-posterior axis (AP axis) at ~512 µm intervals and assessed for total number of M/TCs (Tbx21+ cells) and for percentage of M/TCs expressing both *Kv1.3* and *Insr* (***J***). Each data point represents the average from 5 separate mice, separated by laminar layer and sex. ***K–M:*** Percentage of M/TCs (Tbx21+ cells) expressing *Kv1.3* alone (***K***), *Insr* alone (***L***) or both (***M***). Statistical comparisons for ***K–M*** are Kruskal-Wallis (ANOVA) with Dunn's multiple comparisons test. Each data point represents the average of all six antero-posterior sections from each mouse, one data point per mouse per neurolaminar layer, respectively. $^{*}p < 0.05$, GLM = glomerular layer, EPL = external plexiform layer, GCL = granule cell layer.

402 **Superficial tufted cells are modulated by insulin via the Kv1.3 ion channel**

403 To further explore the complementary physiological role of sTCs, we wanted to determine if
404 their excitability could be modulated by insulin—knowing that MCs are modulated by 0.1 μm
405 insulin (Fadool *et al*., 2000, 2011). After sampling for supra-threshold current, synaptic
406 blockers were added to the bath solution. Evoked APs were established using the threshold
407 current with a P_d = 5000 ms and T_s = 30 s for a 5-min paradigm (10 recordings). A
408 representative set of baseline recordings and an associated raster plot is shown in **Fig. 7A,**
409 prior (left) and subsequent (right) to bath application of insulin for 15 min.
410
411 Insulin significantly reduced the average latency to first spike by ~38% (**Fig. 7B**, sTC pre =
412 1220 $\pm$ 723 ms (11) vs. sTC post = 649 $\pm$ 403 ms (11), paired *t*-test, **p* = 0.0132). On average,
413 insulin also increased the AP frequency by ~98% (**Fig. 7C**, sTC pre = 4.76 $\pm$ 1.76 Hz (11) vs.
414 sTC post = 8.49 $\pm$ 4.98 Hz (11), paired *t*-test, **p* = 0.0381), and decreased the average
415 intraburst interval by ~8% (i.e., the pause between APs within a particular burst) (**Fig. 7D**,
416 sTC pre = 65.1 $\pm$ 13.6 ms (11) vs. sTC post = 60.3 $\pm$ 14.9 ms (11), paired *t*-test, **p* = 0.0136).
417 All statistical tests were performed on non-normalized data, however, plots were generated as
418 normalized paired values to visualize individual cell changes across the sampled cells.
419
420
421
422
423
424
425
426
427
428
429
430

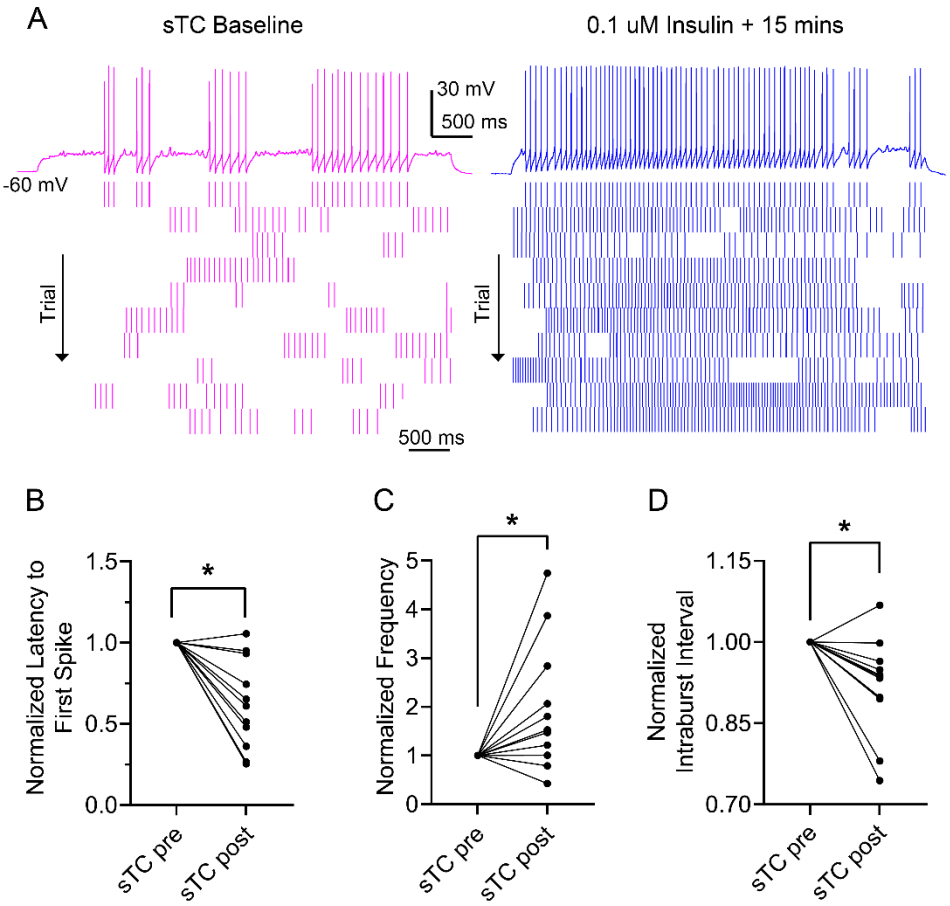

Fig. 7. Bath application of insulin increases spike firing frequency, and shortens latency to first spike and intraburst interval in superficial tufted cells (sTCs). ***A,*** Representative spike trains (***Top***) that were elicited in response to 25 pA current injection while holding the cell near rest (V_h = -60 mV) prior (***Left,*** Baseline) and subsequent (***Right,*** Insulin) to hormone stimulation using P_d = 5 s. (***Bottom***) Representative associated raster plot. Line graph comparing ***B,*** latency to first spike, ***C,*** spike firing frequency, and ***D,*** intraburst interval, prior (pre) and following (post) insulin stimulation in the same cell. Data were analyzed with a paired *t*-test using non-normalized data ***(B)*** **p* = 0.0132, ***(C)*** **p* = 0.0381, and ***(D)*** **p* = 0.0136.

The modulation of MCs by insulin has been shown to depend on the Kv1.3 ion channel using either pharmacological block or targeted gene-deletion (Fadool *et al*., 2000, 2011; Colley *et al*., 2004). Since previous reports demonstrate Kv1.3 expression in sTCs (Kues and Wunder, 1992; Fadool *et al*., 2000; Colley *et al*., 2007), we wanted to determine if insulin modulation of sTCs was also Kv1.3-dependent. Using transgenic mice lacking the *Kv1.3* gene (Kv1.3-/-, see methods) we first compared the AP bursting characteristics between the sTCs of GFP mice (Kv1.3 +/+), and the sTCs of Kv1.3 -/- mice. In accordance with the findings in Kv1.3 -

/- MCs (Fadool *et al*., 2004, 2011; Tucker *et al*., 2010; Thiebaud *et al*., 2016), we found that Kv1.3 -/- sTCs tend to burst more often, and have shorter bursts with faster intraburst frequency. Kv1.3 -/- sTCs also have shorter latency to first spike and faster overall evoked AP frequency than Kv1.3 +/+ sTCs (**Table 2**). Mean values, sample sizes, *p* values, and statistical tests are reported within each column.

	Bursts per 50 s (n)	Spikes per Burst (n)	Burst Duration (ms)	Intraburst Interval (ms)	Intraburst Frequency (Hz)
Kv1.3 +/+ sTCs	24.8 ± 10.0	7.6 ± 3.1	414.6 ± 209.5	65.1 ± 12.9	17.0 ± 5.6
n	11	11	11	11	11
Kv1.3 -/- sTCs	55.0 ± 9.6	6.0 ± 1.4	215.0 ± 82.4	45.6 ± 11.7	26.1 ± 8.7
n	4	4	4	4	4
p-value	**0.0003**	ns (0.2362)	**0.0305**	**0.0291**	**0.0048**
Test used	†	‡	‡	†	₸

	Pause Duration (ms)	Latency to First Spike (ms)	AP Frequency (Hz)	Event Frequency (Hz)	% Bursting Cells
Kv1.3 +/+ sTCs	729.8 ± 354.1	1221.6 ± 689.4	4.8 ± 1.7	7.6 ± 2.6	
n	11	11	11	11	
Kv1.3 -/- sTCs	655.3 ± 210.4	419.5 ± 298.7	7.1 ± 2.2	7.6 ± 2.5	
n	4	5	5	5	
p-value	ns (0.7183)	**0.0090**	**0.0475**	ns (0.7427)	
Test used	†	‡	†	₸	

Table 2. Spike bursting properties in superficial tufted cells (sTCs) compared between wildtype (WT) and Kv1.3 -/- mice. Recordings were made while holding cells near rest (V_h = -60 mV) and injecting 75 pA of current. Data were computed across a 50 s recording period (10, 5s sweeps). Values are mean ± standard deviation. ns = not significant, †= Student's *t*-test, ‡= *t*-test with Welch's correction, ₸= Mann-Whitney U

457

458 Using Kv1.3 -/- mice, we next repeated the previous insulin experiment shown **Fig. 7**. A
459 representative set of baseline recordings and associated raster plot for sTCs evoked APs is
460 shown in **Fig. 8A,** prior (left) and subsequent (right) to bath application of insulin for 15 min
461 as recorded in the Kv1.3-/- mice. Unlike in recordings acquired from Kv1.3 +/+ mice, insulin
462 did not alter latency to first spike (**Fig. 8B**, Kv1.3-/- sTC pre = 420 $\pm$ 334 ms (5) vs. Kv1.3-/-
463 sTC post = 390 $\pm$ 232 ms (5), paired *t*-test, $p = 0.5694$). Insulin also did not affect AP firing
464 frequency (**Fig. 8C**, Kv1.3-/- sTC pre = 7.09 $\pm$ 2.48 Hz (5) vs. Kv1.3-/- sTC post = 7.13 $\pm$
465 2.93 Hz (5), paired *t*-test, $p = 0.9300$, n = 5), nor affect the intraburst interval (**Fig. 8D***,* Kv1.3-
466 /- sTC pre = 45.6 $\pm$ 13.6 ms (4) vs. Kv1.3-/- sTC post = 52.7 $\pm$ 17.8 ms (4), paired *t*-test, $p =$
467 0.1990, n = 4) in Kv1.3-/- mice. The same 5 cells were used for all pre/post comparisons, but
468 one cell did not fire quickly enough for burst analysis (see methods).

469
470
471
472
473
474
475
476
477
478
479
480
481
482
483
484
485

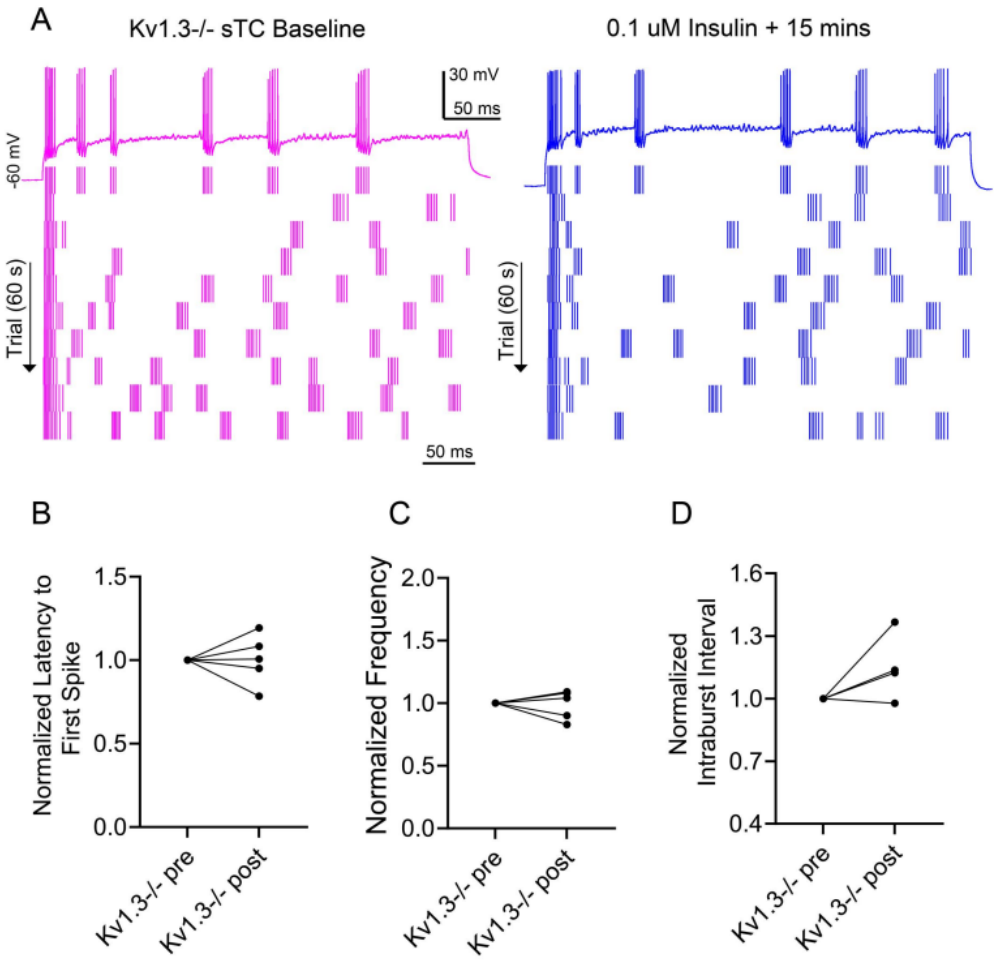

Fig. 8. Insulin fails to modulate spike firing frequency in superficial tufted cells of Kv1.3-/- mice. ***A,*** Representative spike trains (***Top***) and associated raster plot (***Bottom***) recorded as in *Figure 9*. Line graphs Line graph comparing ***B,*** latency to first spike, ***C,*** spike firing frequency, and ***D,*** intraburst interval, prior (pre) and following (post) insulin stimulation in the same cell. Data were analyzed with a paired *t*-test using non-normalized data, $p > 0.05$.

Discussion

We have demonstrated that the two major output neurons in the olfactory bulb have different biophysical properties, despite both neurons expressing IR kinase and exhibiting modulation by insulin. sTCs are more excitable, as evidenced by the lower threshold needed to evoke an AP, a decreased ISI, and a greater AP firing frequency particularly at lower current injection. We found that the APs of sTCs have greater peak amplitude, greater anti-peak amplitude, faster rise kinetics, and faster decay kinetics than those of MCs – while at the same time, the incidence of a train of AP activity was similar between the two output neurons. While there

500 are differences in the voltage dependence of voltage-activated outward currents between MCs
501 and sTCs, both are blocked by the Kv1.3 vestibule blocker, MgTx. We determined that
502 voltage-activated outward currents in sTCs are modulated by insulin, and that the Kv1.3 ion
503 channel is necessary for this modulation.
504
505 Burton and Urban (Burton and Urban, 2014) first compared mitral cell biophysical properties
506 with that of what they called "tufted cells", which were projection neurons whose cell bodies
507 resided in the superficial 50% of the EPL. Prior to their publication, physiologists often
508 clustered mitral and tufted cells together as a homogenous neuronal population (Fadool and
509 Levitan, 1998; Tucker and Fadool, 2002; Youngstrom and Strowbridge, 2015; Liu et al.,
510 2016) due to their similar function as output neurons. Using new nomenclature described by
511 Jones et al. (Jones et al., 2020), we now know that TCs are comprised of a variety of sub-
512 classes that are functionally distinct with differential sensitivity to inhibitory/excitatory
513 circuits to putatively sharpen tuning specificity for odorants during sensory processing (Zhou
514 et al., 2023). The tufted cells first measured by Burton and Urban (2014) likely consisted of a
515 mixed population of sTCs and mTCs. Nonetheless, some of our data measured in strictly
516 sTCs, align well with what they reported for "tufted cells" in general. Burton and Urban found
517 that their TCs had a higher instantaneous frequency (peak instantaneous rate) that differed
518 with current injection magnitude than that of MCs, and that the AP shape of their TCs
519 exhibited a narrower half width (FWHM), a steeper decay slope, and faster time to anti-peak
520 (after-hyperpolarization). Our comparative measurements were quite similar. Thus, we
521 similarly report that sTC have greater intrinsic excitability than that of MCs. Unlike this
522 earlier study, however, we found that the AP shape in sTCs compared with that of MCs, has a
523 greater peak amplitude, steeper maximum rise slope, a greater anti-peak amplitude, and the
524 minimum current necessary to evoke a first AP (threshold) is lower.
525
526 Burton and Urban further found that their TCs were more likely to elicit spike trains (stutter)
527 compared with that of MCs, which they characterized based upon the increased co-efficient of
528 variation of the ISI observed in the TCs. We did not observe a greater overall firing
529 irregularity in our recorded sTCs, and in fact, we found the opposite - our recorded MCs had a
530 greater ISI variance at lower levels of current injection than that of sTC. Also inconsistent

531 with our findings; sTCs and MCs did not have significantly different AP train properties
532 (spikes per train, pause duration, or latency to first spike), nor did sTCs have a statistically
533 higher propensity to elicit a spike train. The likely inclusion of both sTCs and mTCs in their
534 study could account for these differential findings. In fact, Antral et al. (2006) also reports in
535 their study of eTC, that they observed two subclassifications, nonbursting (contained lateral
536 dendrites) and bursting (lacked lateral dendrites), that were found to be both morphologically
537 and functional diverse. We believe that we have complemented the findings of Burton and
538 Urban, expanding upon their comparisons to more specifically characterize selectively the
539 sTCs and not multiple subtypes clustered together.
540
541 Differences in ion channel expression could underlie the greater excitability of sTCs
542 compared to that of MCs. We found voltage-activated currents in the window of -60 to -20
543 mV to be greater in MCs than those of sTCs. It is well known that *shaker* family members
544 have a voltage-activation above -50 to -40 mV (Zagotta and Aldrich, 1990), therefore Kv1.2
545 and Kv1.3 likely are not highly responsible for the difference in voltage-activated currents
546 between the two cell types. This is corroborated by the fact that both cell types exhibited a
547 similar pharmacological response to MgTx and both are shown to be similarly modulated by
548 bath application of insulin, previously demonstrated to be the result of Kv1.3 being used as a
549 substrate for tyrosine phosphorylation in the OB in a use- or activity-dependent manner
550 (Fadool et al., 2000, 2011). We also measured a select slowing of the deactivation kinetics in
551 MCs at the sampled -40 mV hyperpolarizing step that might selectively lower MC excitability
552 vs. that in sTCs. A comparison of MC activity in Kv1.3-/- mice vs. pharmacological block of
553 the channel in the current study, may reveal differences in underlying ion channel expression
554 between sTCs and MCs. The threshold for activation of voltage-activated outward currents in
555 the MCs of Kv1.3-/- mice were previously found to be shifted +20 mV in the positive
556 direction compared to wild-type MCs (Fadool et al., 2004), but these Kv1.3-/- MCs have an
557 upregulation of a *slack* sodium-activated potassium (K_{Na}) channel (Lu et al., 2010), an
558 increase in calcium channel expression (Fadool et al., 2004), and may have increased chloride
559 currents (Koni et al., 2003). Therefore, the threshold for activation of voltage-activated
560 currents in sTCs and Kv1.3-/- MCs is both higher than that of wildtype MCs, but the precise
561 nature of any differences in channel expression (i.e., perhaps sTCs express higher levels of

562 K_{Na} channels than MCs) is not known. This opens the door to a larger area of research that is
563 beyond the scope of this report.
564
565 sTCs are modulated by the presence of insulin, and our data demonstrate that this modulation
566 depends upon the Kv1.3 ion channel. Insulin's primary role in the periphery is to mobilize
567 glucose from the bloodstream following a meal; however, insulin is known to have many roles
568 as a signaling molecule in the central nervous system (CNS). The levels of insulin in the CNS
569 do not mirror the levels of insulin in the periphery, and the highest concentration of insulin
570 receptors and binding affinity to insulin (outside the pancreas) is found in the OB (Baskin et
571 al., 1983; Hill et al., 1986; Gupta et al., 1992; Schwartz et al., 1992; Myers Jr. and White,
572 1993; White, 1997; Wickelgren, 1998; Banks et al., 1999; Fadool et al., 2000; Aimé et al.,
573 2012; Palouzier-Paulignan et al., 2012; Fadool and Kolling, 2020). MCs have an interesting
574 co-localization of IR kinase and Kv1.3 with adaptor proteins that functions to cluster signaling
575 transduction cascades in close proximity (Marks and Fadool, 2007; Marks et al., 2009). In the
576 brain, insulin resistance is implicated in the progression of neurodegeneration and dementia
577 (Kuljiš and Salković-Petrišić, 2011; Arnold et al., 2018; Ferreira et al., 2018; Hong et al.,
578 2021; Femminella et al., 2021). Our report elevates the role of Kv1.3 as a target for the
579 investigation of olfactory function, and, by extent, the complexities of insulin signaling in the
580 OB. Though not annotated directly, previous histological reports suggested expression of
581 Kv1.3 in sTCs. These include Figure 1E from Kues 1992 (Kues and Wunder, 1992), Figure 7
582 from Fadool 2000 (Fadool et al., 2000), and Figure 9 from Colley 2007 (Colley et al., 2007).
583 At this time, we do not know of any reports that previously suggested expression of insulin
584 receptors on sTCs. MCs are known to be modulated by insulin in a similar manner to our sTC
585 findings (Fadool et al., 2000, 2011; Das et al., 2005; Tucker et al., 2010; Aimé et al., 2012;
586 Kuczewski et al., 2014), and this modulation in MCs is known to occur via phosphorylation of
587 Kv1.3 (Bowlby et al., 1997; Fadool and Levitan, 1998; Fadool et al., 2000, 2011).
588
589 While we know that IR kinase is also co-localized with glucagon-like 1 peptide receptors in
590 MCs (Thiebaud et al., 2016) and have discovered an array of neuromodulators that alter Kv1.3
591 channel function and general excitability of these output neurons (Cook and Fadool, 2002;
592 Tucker and Fadool, 2002; Colley et al., 2009; Fadool et al., 2011; Mast and Fadool, 2012;

593 Tucker et al., 2013; Huang et al., 2017; Thiebaud et al., 2019), the possibility of
594 neuromodulation of sTCs remains highly likely and greatly unexplored. Herein, we have
595 distinguished these two output neurons in terms of biophysical function, but there may be a
596 range of neuromodulators that can affect and fine tune odor information coding or regulation
597 of metabolic state (Thiebaud et al., 2016, 2019; Kolling et al., 2022). Moreover, we have
598 recently enhanced total excitability of the output neurons (MCs and all classes of TCs) using
599 cell selective CRISPR genome editing of Kv1.3 to support a new function of the olfactory
600 system – metabolic regulation and energy homeostasis (Kolling et al., 2022). Thus, there is
601 much to discover concerning both the division of olfactory function between MCs and TCs
602 (odor context, valence, vs. odor identity), as well as the combined parallel function of
603 olfactory output neurons in regulating whole-body metabolism.
604

605 # MATERIALS AND METHODS

606 ## Ethical approval

607 All animal procedures were reviewed and approved by Florida State University (FSU)
608 Laboratory Animal Resources (Protocol 202000045) that abided by the American Veterinary
609 Medical Association (AVMA) and the National Institutes of Health (NIH). In preparation for
610 OB slice electrophysiology, mice were anesthetized with isoflurane (Aerrane; Baxter,
611 Deerfield, IL, USA) using the Institutional Animal Care and Use Committee (IACUC)-
612 approved drop method and then were killed by decapitation (AVMA Guidelines on
613 Euthanasia, June 2007). In preparation for histology, mice were anaesthetized with a mixture
614 of ketamine (100 mg/kg body weight) and xylazine (10 mg/kg body weight) prior to
615 intracardial perfusion with 4% paraformaldehyde and euthanasia by decapitation (AVMA
616 Guidelines on Euthanasia, June 2007). Our work was guided by the animal ethics checklist
617 reported by Grundy, 2015 (Grundy, 2015).
618

619 ## Solutions and reagents

620 Salts and sugars, unless otherwise noted, were obtained from Thermo Fisher Scientific
621 (Waltham, MA, USA) or Sigma-Aldrich Chemical (St. Louis, MO, USA). Artificial cerebral
622 spinal fluid (aCSF) contained (in mm): 119 NaCl, 26.2 $NaHCO_3$, 1 NaH_2PO_4, 2.5 KCl, 1.3
623 $MgCl_2$, 2.5 $CaCl_2$ and 22 d-glucose (pH 7.3; 300–310 mOsm). Sucrose-modified aCSF was

624 used for vibratome sectioning and recovery, and contained (in mm): 83 NaCl, 26.2 $NaHCO_3$,
625 1 NaH_2PO_4, 3.3 $MgCl_2$, 0.5 $CaCl_2$, 72 sucrose and 22 d-glucose (pH 7.3; 300-310 mOsm) (Jan
626 and Westbrook, 2007). Slice intracellular (pipette) solution contained (in mm): 135 potassium
627 gluconate, 10 KCl, 10 HEPES (N-2-hydroxyethylpiperazine-N-2-ethane sulfonic acid), 10
628 $MgCl_2$, 0.4 NaGTP and 2 NaATP (pH 7.3; 280–285 mOsm). PBS contained the following (in
629 mm): 136.9 NaCl, 2.7 KCl, 10.1 Na_2HPO_4, and 1.8 KH_2PO_4 (pH 7.4). Paraformaldehyde
630 (PFA) for tissue fixation consisted of 4% PFA (Eastman Kodak, Rochester, NY, USA) in
631 PBS. Blocking buffer and incubation buffer consisted of 2% bovine serum albumin fraction V
632 (BSA) (Invitrogen, Waltham, MA, USA) and 0.2% Tween-20 (Fisher, Hampton, NH, USA)
633 in 1X PBS (Salameh et al., 2017).
634
635 The following synaptic blockers and channel vestibule blocker were prepared as concentrated
636 stock solutions in aCSF, stored at -20ºC until day of use, and then diluted to the following
637 working concentrations: 10 µM gabazine (catalog #104104-50-9, MilliporeSigma, Burlington,
638 MA, USA), 5 µM 2,3-dioxo-6-nitro-7-sulfamoyl-benzo[f]quinoxaline (NBQX, catalog
639 #ab120045, Abcam, Waltham, MA, USA), 25 µM (2R)-amino-5-phosphonovaleric acid (AP5,
640 catalog #ab120003, Abcam), 1 nM margatoxin (MgTx, catalog # M8278, MilliporeSigma),
641 0.1 uM insulin (Fadool et al., 2011*a*) (catalog #I2643, MilliporeSigma), and 100 nM
642 tetrodotoxin (TTX, catalog # 120055, Abcam). Prior to use, MgTx and insulin were
643 additionally mixed with 0.05% bovine serum albumin (BSA fraction V, catalog # BSAV-RO,
644 Sigma-Aldrich) to prevent loss of peptide to tubing and plasticware while recording.
645
646 **Animals**
647 All mice were housed at the FSU vivarium on a standard 12 h/12 h light/dark cycle and in
648 accordance with institutional requirements for animal care. Mice were individually housed in
649 conventional-style rodent cages containing separate food and water that could be obtained *ad*
650 *libitum*. Mice were maintained on chow that was comprised of 13.5% kcal fat, 59.1% kcal
651 carbohydrate, and 28.05% kcal protein (Catalog #5001, Purina Company, St. Louis, MO,
652 USA).
653

654 B6:CBA-Tg(Tbx21-cre)1Dlc/J mice with cre recombinase expression limited to mitral and
655 tufted cells (catalog #024507, Jackson Labs, Bar Harbor, ME, USA;
656 RRID:IMSR_JAX:024507) were crossed with B6J.129(B6N)-Gt(ROSA)26Sor$^{tm1(CAG\text{-}cas9^{\wedge},\text{-}}$
657 $^{EGFP)Fezh}$/J mice (catalog #026175, Jackson Labs; RRID:IMSR_JAX:026175) to generate
658 progeny mice with bicistronic spCas9/EGFP expression limited to the mitral and tufted cells.
659 The EGFP signal, along with anticipated physiological parameters, was used to identify mitral
660 vs. tufted cells (Chen and Shepherd, 1997; Marks *et al*., 2009). A total of 76 Tbx21-cre x
661 Cas9/EGFP male and female mice were used in our experiments for electrophysiology and
662 RNAscope (referred to as simply 'GFP mice' throughout) and ranged from 19 to 28 postnatal
663 days (PD) in age.
664
665 Kv1.3-/- mice were crossed with Thy1-YFP mice to generate progeny mice with
666 fluorescently-labeled OB neurons. Kv1.3-/- mice (RRID:IMSR_JAX:027392) were produced
667 previously by excision of the N-terminal one-third of the *Kv1.3* gene (Xu et al., 2003; Koni et
668 al., 2003) and were a generous gift from Drs. Leonard Kaczmarek and Richard Flavel (Yale
669 University, New Haven, CT, USA). Thy1-YFP mice (RRID:IMSR_JAX:014130) were a gift
670 from Dr. Gouping Feng (MIT Broad Institute, Boston, MA, USA) (Feng et al., 2000). A total
671 of 5 Kv1.3-/- x YFP male and female progeny mice were used for electrophysiology (referred
672 to as simply 'Kv1.3-/- mice' throughout) and ranged from PD19-28 in age.
673

674 **Olfactory bulb slice recordings**

675 OB slices for electrophysiological recordings were acquired from GFP or Kv1.3-/- mice as
676 described previously (Fadool et al., 2011; Mast and Fadool, 2012; Huang et al., 2017;
677 Thiebaud et al., 2019; Kolling et al., 2022). Briefly, mice were anesthetized by inhalation of
678 isoflurane, quickly decapitated, and the OBs were rapidly exposed by removing the dorsal and
679 lateral portions of the skull (Nickell et al., 1996). The OBs (while still attached to the
680 forebrain) were quickly removed, glued to a sectioning block with Superglue (Lowe's Home
681 Improvement, Tallahassee, FL, USA) and submerged in oxygenated (95% O_2/5%CO_2), ice-
682 cold, sucrose-modified artificial cerebral spinal fluid (aCSF) to prepare the tissue for
683 sectioning. Coronal sections (300 μm) were cut in oxygenated, ice-cold, sucrose-modified
684 aCSF using a Series 1000 Vibratome (Leica, Wetzlar, Germany; RRID:SCR_016495). The

685 OB sections were allowed to recover in an interface chamber (Krimer and Goldman-Rakic,
686 1997) with oxygenated, sucrose-modified aCSF at 33° C for 15 min and then were maintained
687 at room temperature (rt) in oxygenated normal aCSF until needed (Fadool *et al*., 2011). OB
688 slices were recorded in a continuously-perfused (Ismatec; 1-2 ml/min), submerged-slice
689 recording chamber (RC-26, Warner Instruments, Hamden, CT, USA) with aCSF at rt.
690
691 OB slices were visualized at 10x and 40x using an Axioskop 2FS Plus Microscope (Carl Zeiss
692 Microimaging, Thornwood, NY, USA) equipped with fluorescent excitation and infrared
693 detection capabilities (CCD100; Dage-MTI, Michigan City, IN, USA). Electrodes were
694 fabricated from borosilicate glass (#1405002; Hilgenberg GmbH, Malsfeld, Germany) to a
695 diameter of ~2 μm to yield pipette resistances ranging from 4 to 8 MΩ. Positive pressure was
696 retained when navigating through the OB laminae until a high resistance seal (1.5–10 GΩ)
697 was obtained on a positionally-identified MC or sTC in the slice (Fadool et al., 2011). The
698 morphology and biophysical properties of the neurons were used to distinguish MCs and sTCs
699 (Nickell et al., 1996; Schoppa and Westbrook, 2001; Fadool et al., 2004; Fadool and Kolling,
700 2020). MCs were selected only if > 50% of their cell body resided within the MCL. sTCs
701 were selected only if their cell body resided in the outer one-third of the EPL, and were not
702 selected if their cell body partially resided within the GLM. In addition, GFP mice provided
703 fluorescent markers that served as secondary confirmation of cell identity, and were readily
704 distinguishable. The cell-attached configuration was established by applying gentle suction to
705 the lumen of the pipette while monitoring resistance. Whole-cell access was obtained by
706 applying a 100 ms, 1 mV pulse across the membrane while applying sharp suction to the
707 lumen of the pipette. Membrane voltage and current properties were generated using
708 pCLAMP, version 9 or 10, in conjunction with a Multiclamp 700B amplifier (Axon
709 Instruments; RRID:SCR_011323/Molecular Devices; RRID:SCR_018455). The analog signal
710 was filtered at 3 kHz and minimally digitally sampled every 100 μs with a Digidata 1440A
711 digitizer (Axon Instruments, Molecular Devices; RRID:SCR_021038). The pipette
712 capacitance was electrically compensated through the capacitance neutralization circuit of the
713 Multiclamp 700B amplifier. Resting membrane potentials were corrected for a calculated -7
714 mV junction potential offset. Membrane capacitance was acquired from the membrane test
715 function of Clampex 10.7 (Axon Instruments, RRID:SCR_011323). Input resistance was

716 calculated using Ohm's law by injecting a -50 pA current and measuring the induced voltage
717 deflection. For clarity across disciplines, this report uses the electrophysiological terminology
718 that is used by the pCLAMP software suite. Where applicable, other common names are
719 included in parentheses.
720
721 After establishing a whole-cell configuration, cells were first sampled for adequate resting
722 potential (less than -50 mV), proper access resistance (less than 40 MΩ), and adequate input
723 resistance (greater than 150 MΩ) prior to initiating either a series of current- or voltage-clamp
724 recordings. For current-clamp recordings, cells were held at -60 mV (near rest; V_h) between
725 pulses to compare data across cells. Peri-threshold current levels were determined by
726 incrementally injecting a family of current pulses of 1000 millisecond (ms) duration (P_d).
727 Current was injected every 30 seconds (s) and was stepped in 25 pA increments from -50 pA
728 to 175 pA to obtain action potential (AP) characteristics and current-dependence data.
729 Following the determination of spike threshold, cells were stimulated with 10 super-threshold
730 sweeps using a P_d of 5000 ms (typically ranging from 15 to 150 pA) every 30 s (T_s) to acquire
731 spike frequency and latency data. Current-clamp data were acquired in the presence of
732 synaptic blockers and voltage-clamp data were acquired in the presence of 20 μM TTX to
733 eliminate unwanted AP spiking (see Solutions).
734
735 AP characteristics, latency to first spike, spike event frequency, interspike interval, intratrain
736 interval, and spike train length were measured using Clampfit software as described
737 previously (Balu et al., 2004; Fadool et al., 2011; Mast and Fadool, 2012). A train was defined
738 as three or more consecutive spikes within a period of 100 ms or less, as established by Balu
739 et al. (Balu et al., 2004). M/TC firing is intrinsically intermittent and is characterized by
740 variable train characteristics. As such, classical means of computing spike timing variability,
741 such as peri-stimulus time histograms, were less suitable for the behavior of these neurons.
742 Therefore, alternative means of spike analysis were applied as described previously (Balu et
743 al., 2004; Fadool et al., 2011; Thiebaud et al., 2016; Kolling et al., 2022). For voltage-clamp
744 recordings, cells were held at -80 mV (V_h), then stepped from -100 mV to +40 mV (V_c) in
745 +20 mV increments for a duration of 400 ms (P_d) with a stimulation interval (T_s) of 45 s.
746

747 **RNA scope and quantification**

748 Five male and five female GFP mice (10 mice total) were anesthetized with ketamine/xylazine
749 and fixed via transcardial perfusion of PBS followed by 4% PFA. Brains were cryoprotected
750 in 30% sucrose before being embedded in OCT and flash frozen. Mouse brains were
751 cryosectioned coronally at 16 µm, and sections were collected 1:10. Sections were mounted
752 on histobond glass slides, and RNAscope was performed according to the ACDbio
753 manufacturer's protocol using commercially available probes for *GFP, Kv1.3* and *Insr*. The
754 sequence of the mouse *GFP* transgene was used to verify the selection of GFP RNAscope
755 probe. Images were acquired using an Olympus VS200 slidescanner at 20X, and analysis was
756 performed using QuPath software (v 0.5). The 'cell detection' function was first used to
757 identify Tbx21+ cells, then object classifiers were created for *Kv1.3* and *Insr* using a threshold
758 for mean fluorescent intensity within each cell. Validation of this workflow was performed
759 manually, once per neurolaminar layer (MCL, EPL, and GLM).
760

761 **Experimental design and statistical analyses**

762 Before performing any statistical comparisons, data were first analyzed with the Dixon's Q
763 test to identify any outliers. Data were then checked for normal distribution and homogeneity
764 of variance using the Fmax test. Analysis of data collected did not identify any outliers.
765 Where collected data violated homogeneity of variance (failed the Fmax test), the selection of
766 applied statistics was changed to the nonparametric equivalent. Paired comparisons (innate
767 properties, action potential kinetics, bursting metrics) were analyzed using Student's *t* test or
768 Mann-Whitney U at the 95% confidence level ($\alpha < 0.05$). There were no sex-specific
769 differences in the measured parameters, so measurements from both sexes were combined. IV
770 plots, frequency and interspike interval (ISI) were analyzed using a mixed two-way RM
771 ANOVA with current and voltage as factors (IV) or current and cell type as factors (frequency
772 and ISI); at the 95% confidence level ($\alpha < 0.05$). Modulation of voltage-activated current
773 between cell types was analyzed using a mixed three-way RM ANOVA with voltage, cell
774 type, and drug as factors; at the 95% confidence level ($\alpha < 0.05$). Insulin modulation data
775 were analyzed using within-cell comparisons by applying a paired *t* test at the 95% confidence
776 level ($\alpha < 0.05$). Categorical AP spike train type analysis was performed using a Chi-Square
777 test, where the expected proportion of sTCs eliciting spike trains was set as the observed

778 proportion of MCs eliciting spike trains; 95% confidence level ($\alpha < 0.05$). For the two-way
779 RM ANOVA tests, the Sidak method for multiple comparison testing was used as the post-
780 hoc analysis to make mean-wise comparisons between cell types or between drug treatments.
781 All reported values in the text represent the mean ± SD. Figures largely report individual data
782 points using violin graphs and represent number of cells as noted in the figure legends.
783 Sample sizes for the line graphs are reported in the figure legends. Where means are reported
784 in the figures, the error is reported as the SEM. Individual *p* values are reported for each
785 experiment within the corresponding graph with the individual F statistic described in the
786 results section. Statistical tests were performed using GraphPad Prism 9 (GraphPad Software)
787 while the graphs and figures were produced using a combination of Origin v8 (OriginLab
788 Corporation; RRID:SCR_014212), Adobe Photoshop CS4 (Adobe; RRID:SCR_014199), and
789 GraphPad Prism 9 (GraphPad Software; RRID:SCR_002798).
790
791 All electrophysiological data were analyzed using pClamp, version 10 (Clampfit 10.7;
792 Molecular Devices; RRID:SCR_011323) and Igor Pro, version 6.12A (WaveMetrics Inc.;
793 RRID:SCR_000325) with the plug-in NeuroMatic, version 2 (written by Jason Rothman;
794 http://www.neuromatic.thinkrandom.com; RRID:SCR_004186). Exact *p* values, statistical
795 tests, and parameters are given in the results text/figures for each data set. Specific variables
796 required for independent replication (sample size, number of animals, etc.) and full statistical
797 reporting can be found in the methods and results text/figures for each respective experiment
798 and the supplemental statistical table (Supplemental Table 1).
799

800 **Figure Legends**

801 **Fig. 1**. **Categorization and interactions of the principal projection neurons of the olfactory**
802 **bulb.** The olfactory bulb neurolamina is divided across the glomerular layer (GLM), external
803 plexiform layer (EPL), the mitral cell layer (MCL), and the innermost granule cell layer (GCL). Also
804 shown is the olfactory mucosa containing the olfactory sensory neurons (OSNs). This schematic
805 highlights the four classes of output or projection neurons, namely the external tufted cells (eTCs,
806 pink), the superficial tufted cells (sTCs, gray), the middle tufted cells (mTCs, purple), and the mitral
807 cells (MCs, red). The soma of the eTCs are found within the GLM. The sTC soma reside in the
808 superficial one-third of the EPL. The deep two-thirds of the EPL contain both the mTCs and
809 misplaced MCs. The MCL houses the eponymous MCs. Blue plus signs (+) represent excitatory
810 synapses, red minus signs (-) represent inhibitory synapses, and pink plus signs (+) represent
811 excitatory dendro-dendritic interactions originating from external tufted cells (eTCs). Reciprocal
812 synapses are denoted by a double arrow. PG = periglomerular cell, sSAC = superficial short axon
813 cell, EPLi = interneuron of the external plexiform layer, GCL = granule cell layer, GC = granule cell,
814 PPG = preproglucagon neuron, dSAC = deep short axon cell. *Modified from Huang* et al. *2021.*

815 **Fig. 2.** Outward voltage-activated current properties of mitral cells and superficial tufted cells. ***A,***
816 Family of voltage-activated currents, V_h = -80 mV where V_c was stepped in 20 mV increments from -
817 100 mV to +40 mV using a P_d = 400 ms. Colored sweeps correspond to significantly different
818 colored data points in (***B***). ***B,*** Normalized IV plots (2-w mixed RM ANOVA, cell type ***p =
819 0.0056, Sidak's post-hoc test, $^{\#}p < 0.05$, $^{\#\#}p < 0.01$; voltage x cell type interaction ****$p < 0.0001$).
820 ***C,*** Violin plot of non-normalized peak transient voltage-activated current at +40 mV, Mann-Whitney
821 U. Violin plot of the *Tau* of inactivation (*left*) and deactivation (*right*) at **(D)** Vc = -40 mV and **(E)**
822 +40 mV, respectively, Mann-Whitney U (*p = 0.0107). MC = mitral cell population sampled, sTC =
823 superficial tufted cell population sampled.

824 **Fig. 3.** Sensitivity of mitral and superficial tufted cells to a selective blocker of Kv channels. ***A,***
825 Family of voltage-activated currents recorded as in Figure 3 prior (***Top*,** Baseline) and following
826 (***Bottom*,** +1 nM MgTx) 15-min bath application of margatoxin (MgTx) in a representative ***A,*** mitral
827 cell (MC) and ***B,*** superficial tufted cell (sTC). ***C,*** Normalized IV plots prior (solid symbols) and
828 following (open symbols) bath application of MgTx in a population of MCs (***Left,*** 2-w mixed RM
829 ANOVA, drug F (1, 9) = 43.62, ****$p < 0.0001$, with a Sidak's post hoc test, $^{\#\#\#}p = 0.0008$, $^{\#\#\#\#}p <$
830 0.0001; voltage x drug interaction F (7, 63) = 43.86, ****$p < 0.0001$) and a population of sTCs
831 (***Right,*** 2-w mixed RM ANOVA, drug ***p = 0.0003, Sidak's post-hoc test, $^{\#\#\#\#}p < 0.0001$; voltage x
832 drug interaction ****$p < 0.0001$). ***C, Bottom*** **–** 3-way mixed RM ANOVA result comparing the two
833 IV plots in ***C, Left-Right*** (3-w mixed RM ANOVA, voltage x cell type interaction F (7, 123) = 3.879,
834 ***p = 0.0008; voltage x drug interaction F (7, 123) = 57.42, ****$p < 0.0001$; cell type x drug
835 interaction F (1, 123) = 0.4244, p = 0.5160; voltage x cell type x drug interaction F (7, 123) = 0.7633,
836 p = 0.6190).

837 **Fig. 4**. Spike firing properties compared between mitral cells (MC) and superficial tufted cells (sTC).
838 ***A*,** Representative action potential trains evoked by various current steps as indicated, recorded from
839 a MC (***Left***) vs. sTC (***Right***). ***B,*** Violin plot comparing the current needed to evoke action potentials
840 (rheobase), Mann-Whitney U, **p = 0.0021. Line plots for ***C,*** mean spike frequency across current
841 step and ***D,*** mean interspike interval (ISI). Line plot data were analyzed with a ***(C)*** 2-w mixed RM
842 ANOVA, cell type **p = 0.0011; current x cell type interaction ***p = 0.0009, Sidak's post-hoc test,

843 $^{\$\$}p < 0.01$, $^{\$\$\$}p < 0.001$, ***(D)*** 2-w mixed RM ANOVA, cell type ****$p < 0.0001$; current x cell type
844 interaction ****$p < 0.0001$, Sidak's post-hoc test, $^{\#}p < 0.05$, $^{\#\#}p < 0.01$.

845 **Fig. 5.** Action potential shape and spike train activity compared between mitral cells (MC) and
846 superficial tufted cells (sTC). Line plot for ***A,*** maximum decay slope (max decay slope) and ***B,*** time
847 to achieve maximum decay slope from peak magnitude (time to max decay slope) across current step.
848 Line plot data were analyzed with **(A),** 2-w mixed RM ANOVA, cell type *p = 0.0186, Sidak's post-
849 hoc test, ##p < 0.01, ###p < 0.001; current x cell type interaction ****p < 0.0001, **(B),** 2-w mixed
850 RM ANOVA, cell type *p = 0.0486, Sidak's post-hoc test, #p < 0.05, ##p < 0.01, ###p < 0.001. ***C,***
851 Representative pair of action potentials recorded in response to a 75 pA current injection held near
852 rest (Vh = -60 mV). ***D,*** Representative raster plot for a cell stimulated with a 50-pA current injection
853 using a P_d = 5 s for each cell type, respectively. Successive trials are stacked vertically below. Violin
854 plots computed across a 50 s recording period (10, 5s sweeps) compare ***E,*** mean number of bursts, ***F,***
855 mean spikes per train, ***G,*** mean pause duration between trains, and ***E,*** mean latency to first spike. ***E-F,***
856 were analyzed using a Student's *t*-test, ***G-H*** were analyzed using Mann-Whitney U; $p > 0.05$. ***I,***
857 Relative proportion of cells eliciting spike train behavior among sampled MCs (***Left***) and sTCs
858 (***Right***), respectively (Chi-squared test, p = .40061, $X^2 = 0.7065$, n = 51).

859 **Fig. 6.** Colocalization of M/TCs with the Kv1.3 channel (*Kv1.3*) and insulin receptor (*Insr*) using
860 RNAscope. Photomicrographs demonstrating neurolaminar distribution of Tbx21 reporter expression
861 (green, ***A***), *Kv1.3* expression (magenta, ***B***), and *Insr* expression (yellow, ***C***), separately and merged
862 (white, ***D***). ***E–H***: Same as ***A–D***, but to demonstrate localization to sTCs with the inclusion of a DAPI
863 nuclear stain. ***I:*** Coronal sections were sampled along the anter-posterior axis (AP axis) at ~512 µm
864 intervals and assessed for total number of M/TCs (Tbx21+ cells) and for percentage of M/TCs
865 expressing both *Kv1.3* and *Insr* (***J***). Each data point represents the average from 5 separate mice,
866 separated by laminar layer and sex. ***K–M:*** Percentage of M/TCs (Tbx21+ cells) expressing *Kv1.3*
867 alone (***K***), *Insr* alone (***L***) or both (***M***). Statistical comparisons for ***K–M*** are Kruskal-Wallis (ANOVA)
868 with Dunn's multiple comparisons test. Each data point represents the average of all six antero-
869 posterior sections from each mouse, one data point per mouse per neurolaminar layer, respectively. $^{*}p$
870 < 0.05, GLM = glomerular layer, EPL = external plexiform layer, GCL = granule cell layer.

871 **Fig. 7.** Bath application of insulin increases spike firing frequency, and shortens latency to first spike
872 and intraburst interval in superficial tufted cells (sTCs). ***A,*** Representative spike trains (***Top***) that
873 were elicited in response to 25 pA current injection while holding the cell near rest (V_h = -60 mV)
874 prior (***Left,*** Baseline) and subsequent (***Right,*** Insulin) to hormone stimulation using P_d = 5 s.
875 (***Bottom***) Representative associated raster plot. Line graph comparing ***B,*** latency to first spike, ***C,***
876 spike firing frequency, and ***D,*** intraburst interval, prior (pre) and following (post) insulin stimulation
877 in the same cell. Data were analyzed with a paired *t*-test using non-normalized data ***(B)*** $*p = 0.0132$,
878 ***(C)*** $*p = 0.0381$, and ***(D)*** $*p = 0.0136$.

879 **Fig. 8.** Insulin fails to modulate spike firing frequency in superficial tufted cells of Kv1.3-/- mice. ***A,***
880 Representative spike trains (***Top***) and associated raster plot (***Bottom***) recorded as in *Figure 9*. Line
881 graphs Line graph comparing ***B,*** latency to first spike, ***C,*** spike firing frequency, and ***D,*** intraburst
882 interval, prior (pre) and following (post) insulin stimulation in the same cell. Data were analyzed with
883 a paired *t*-test using non-normalized data, $p > 0.05$.

884 **Table 1.** Action potential shape compared between mitral cells (MCs) vs. superficial tufted cells
885 (sTCs). Recordings were made while holding cells near rest (V_h = -60 mV) and injecting 75 pA of

current. Values are mean ± standard deviation. ns = not significant, †= Student's *t*-test, ‡= *t*-test with Welch's correction, ⊤= Mann-Whitney U.

Table 2. Spike bursting properties in superficial tufted cells (sTCs) compared between wildtype (WT) and Kv1.3 -/- mice. Recordings were made while holding cells near rest (V_h = -60 mV) and injecting 75 pA of current. Data were computed across a 50 s recording period (10, 5s sweeps). Values are mean ± standard deviation. ns = not significant, †= Student's *t*-test, ‡= *t*-test with Welch's correction, ⊤= Mann-Whitney U

ACKNOWLEDGEMENTS

We would like to thank Carley Huffstetler, Alexis Cox, and Tyla Dolezel for routine technical assistance and in maintaining mouse colonies. We would like to thank Jaime White-James for the oversight of our animal husbandry and routine mouse care needs.

COMPETING INTERESTS

The authors have no interests to declare, scientific or financial.

AUTHOR CONTRIBUTIONS

All authors critically evaluated the work for important intellectual content. All authors acquired, analyzed, or interpreted data in the study. As such, we confirm that all approved the final version of the manuscript; agreed to be accountable for all aspects of the work in ensuring that questions related to the accuracy or integrity of any part of the work are appropriately investigated and resolved; and all persons designated as authors qualify for authorship, and all who qualify for authorship are listed. In using the CRediT (Contributor Roles Taxonomy) guidelines, L.K. and D.F. were responsible for project conceptualization, data curation, formal analysis, funding acquisition, methodology, validation, visualization, and writing the original draft, reviewing, and editing. L.K. was responsible for electrophysiological recordings. C.M. and D.F. were responsible for project administration and supervision. L.K., C.M. and D.F. were responsible for the provision of resources.

FUNDING

This work was supported by the United States Department of Agriculture NIFA Predoctoral Fellowship 2019-07151, an endowment from the Robinson Family and the Tallahassee

Memorial Hospital, a grant from the Higher Education Emergency Relief Fund (HEERF II), a grant from the National Institute on Aging (NIA) at NIH as F32AG084196, and a grant from the National Institute of Diabetes, and Digestive and Kidney Diseases (NIDDK) at NIH as R01DK133464.

DATA AVAILABILITY

All data referenced in this report are summarized in the primary figures contained in the publication. All summarized electrophysiological recordings data are stored in the Fadool Laboratory and are available upon request.

REFERENCES

Aimé P, Hegoburu C, Jaillard T, Degletagne C, Garcia S, Messaoudi B, Thevenet M, Lorsignol A, Duchamp C, Mouly AM and Julliard AK (2012). A physiological increase of insulin in the olfactory bulb decreases detection of a learned aversive odor and abolishes food odor-induced sniffing behavior in rats. *PLoS One* **7,** e51227–e51227.

Antal M, Eyre M, Finklea B and Nusser Z (2006). External tufted cells in the main olfactory bulb form two distinct subpopulations. *Eur J Neurosci* **24(4),** 1124-1136.

Arnold SE, Arvanitakis Z, Macauley-Rambach SL, Koenig AM, Wang H-Y, Ahima RS, Craft S, Gandy S, Buettner C, Stoeckel LE, Holtzman DM and Nathan DM (2018). Brain insulin resistance in type 2 diabetes and Alzheimer disease: Concepts and conundrums. *Nature Rev Neurol* **14,** 168–181.

Balu R, Larimer P and Strowbridge BW (2004). Phasic stimuli evoke precisely timed spikes in intermittently discharging mitral cells. *J Neurophysiol* **92,** 743–753.

Banks WA, Kastin AJ and Pan W (1999). Uptake and degradation of blood-borne insulin by the olfactory bulb. *Peptides* **20,** 373–378.

Bartok A, Toth A, Somodi S, Szanto TG, Hajdu P, Panyi G and Varga Z (2014). Margatoxin is a non-selective inhibitor of human Kv1.3 K+ channels. *Toxicon* **87,** 6–16.

Baskin DG, Porte Jr. D, Guest K and Dorsa DM (1983). Regional concentrations of insulin in the rat brain. *Endocrinol* **112,** 898–903.

Biju KC, Marks DR, Mast TG and Fadool DA (2008). Deletion of voltage-gated channel affects glomerular refinement and odorant receptor expression in the mouse olfactory system. *J Comp Neurol* **506,** 161–179.

950 Bowlby MR, Fadool DA, Holmes TC and Levitan IB (1997). Modulation of the Kv1.3 potassium
951 channel by receptor tyrosine kinases. *J Gen Physiol* **110,** 601–610.

952 Burry RW (2011). Controls for immunocytochemistry: An update. *J Histochem Cytochem* **59,** 6.

953 Burton SD and Urban NN (2014). Greater excitability and firing irregularity of tufted cells underlies
954 distinct afferent-evoked activity of olfactory bulb mitral and tufted cells. *J Physiol* **592,** 2097.

955 Chen F, He A, Tang Q, Li S, Liu X, Yin Z, Yao Q, Yu Y and Li A (2024). Cholecystokinin-
956 expressing superficial tufted cells modulate odour representation in the olfactory bulb and
957 olfactory behaviours. *J Phyiol* **602(14),** 3519-3543.

958 Chen R and Chung SH (2014). Binding modes of two scorpion toxins to the voltage-gated potassium
959 channel kv1.3 revealed from molecular dynamics. *Toxins (Basel)* **6,** 2149–2161.

960 Coecke S, Balls M, Bowe G, Davis J, Gstraunthaler G, Hartung T, Hay R, Merten OW, Price A,
961 Schechtman L, Stacey G and Stokes W (2005). Guidance on good cell culture practice. A report
962 of the second ECVAM task force on good cell culture practice. *Altern Lab Anim* **33,** 261–287.

963 Colley B, Tucker K and Fadool DA (2004). Comparison of modulation of Kv1.3 channel by two
964 receptor tyrosine kinases in olfactory bulb neurons of rodents. *Recept Channels* **10,** 25–36.

965 Colley BS, Biju KC, Visegrady A, Campbell S and Fadool DA (2007). Neurotrophin B receptor
966 kinase increases Kv subfamily member 1.3 (Kv1.3) ion channel half-life and surface expression.
967 *Neuroscience* **144,** 531–546.

968 Colley BS, Cavallin MA, Biju K, Marks DR and Fadool DA (2009). Brain-derived neurotrophic
969 factor modulation of Kv1.3 channel is disregulated by adaptor proteins Grb10 and nShc. *BMC*
970 *Neurosci* **10,** 8.

971 Cook KK and Fadool DA (2002). Two adaptor proteins differentially modulate the phosphorylation
972 and biophysics of Kv1.3 ion channel by Src kinase. *J Biol Chem* **277,** 13268–13280.

973 Das P, Parsons AD, Scarborough J, Hoffman J, Wilson J, Thompson RN, Overton JM and Fadool
974 DA (2005). Electrophysiological and behavioral phenotype of insulin receptor defective mice.
975 *Physiol Behav* **86,** 287–296.

976 Fadool DA, Holmes TC, Berman K, Dagan D and Levitan IB (1997). Tyrosine phosphorylation
977 modulates current amplitude and kinetics of a neuronal voltage-gated potassium channel. *J*
978 *Neurophysiol* **78,** 1563–1573.

979 Fadool DA and Kolling LJ (2020). Role of olfaction for eating behavior. In *The Senses: A*
980 *Comprehensive Reference*, Second Edi., ed. Fritzsch B and Meyerhof W, pp. 675–716. Elsevier.

981 Fadool DA and Levitan IB (1998). Modulation of olfactory bulb neuron potassium current by
982 tyrosine phosphorylation. *J Neurosci* **18,** 6126–6137.

983 Fadool DA, Tucker K and Pedarzani P (2011). Mitral cells of the olfactory bulb perform metabolic
984 sensing and are disrupted by obesity at the level of the Kv1.3 ion channel. *PLoS One* **6,** e24921.

985 Fadool DA, Tucker K, Perkins R, Fasciani G, Thompson RN, Parsons AD, Overton JM, Koni PA,
986 Flavell RA and Kaczmarek LK (2004). Kv1.3 channel gene-targeted deletion produces "Super-
987 Smeller Mice" with altered glomeruli, interacting scaffolding proteins, and biophysics. *Neuron*
988 **41,** 389–404.

989 Fadool DA, Tucker K, Phillips JJ and Simmen JA (2000). Brain insulin receptor causes activity-
990 dependent current suppression in the olfactory bulb through multiple phosphorylation of Kv1.3.
991 *J Neurophysiol* **83,** 2332–2348.

992 Femminella GD *et al*. (2021). Does insulin resistance influence neurodegeneration in non-diabetic
993 Alzheimer's subjects? *Alzheimer's Res & Ther* **13,** 1–11.

994 Feng G, Mellor RH, Bernstein M, Keller-Peck C, Nguyen QT, Wallace M, Nerbonne JM, Lichtman
995 JW and Sanes JR (2000). Imaging neuronal subsets in transgenic mice expressing multiple
996 spectral variants of GFP. *Neuron* **28,** 41–51.

997 Ferreira LSS, Fernandes CS, Vieira MNN and De Felice FG (2018). Insulin resistance in Alzheimer's
998 disease. *Front Neurosci* **12,** 830.

999 Gadiwalla, S, Guillaume C, Huang L, White SJB, Basha N, Petersen PH and Galliano E (2025) *Ex*
1000 *vivo* functional characterization of mouse olfactory bulb projection neurons reveals a
1001 heterogeneous continuum. *eNeuro* 12(3), ENEURO.0407-24.2025.

1002 Garcia ML, Hanner M, Knaus HG, Koch R, Schmalhofer W, Slaughter RS and Kaczorowski GJ
1003 (1997). Pharmacology of potassium channels. *Adv Pharmacol* **39,** 425–471.

1004 Garcia-Calvo M, Leonard RJ, Novick J, Stevens SP, Schmalhofer W, Kaczorowski GJ and Garcia
1005 ML (1993). Purification, characterization, and biosynthesis of margatoxin, a component of
1006 Centruroides margaritatus venom that selectively inhibits voltage-dependent potassium
1007 channels. *J Biol Chem* **268,** 18866–18874.

1008 Gire DH, Franks KM, Zak JD, Tanaka KF, Whitesell JD, Mulligan AA, Hen R and Schoppa NE
1009 (2012). Mitral cells in the olfactory bulb are mainly excited through a multistep signaling path. *J*
1010 *Neurosci* **32,** 2964–2975.

1011 Grundy D (2015). Principles and standards for reporting animal experiments in The Journal of
1012 Physiology and Experimental Physiology. *J Physiol* **593,** 2547–2549.

1013 Gupta G, Azam M and Baquer NZ (1992). Modulation of rat brain insulin receptor kinase activity in
1014 diabetes. *Neurochem Int* **20,** 487–492.

1015 Hayar A, Karnup S, Shipley MT and Ennis M (2004a). Olfactory bulb glomeruli: External tufted
1016 cells intrinsically burst at theta frequency and are entrained by patterned olfactory input. *J*
1017 *Neurosci* **24(5),** 1190-1199.

1018 Hayar A, Karnup S, Ennis M and Shipley MT (2004b). External tufted cells: A major excitatory
1019 element that coordinates glomerular activity. *J Neurosci* **24,** 6676–6685.

1020 Hayar A, Shipley MT and Ennis M (2005) Olfactory bulb external tufted cells are synchronized by
1021 multiple intraglomerular mechanisms. *J Neurosci* **25(36),** 8197-8208.

1022 Hill JM, Lesniak MA, Pert CB and Roth J (1986). Autoradiographic localization of insulin receptors
1023 in rat brain: Prominence in olfactory and limbic areas. *NeuroSci* **17,** 1127–1136.

1024 Holmes TC, Fadool DA and Levitan IB (1996). Tyrosine phosphorylation of the Kv1.3 potassium
1025 channel. *J Neurosci* **16,** 1581–1590.

1026 Hong S, Han K and Park C-Y (2021). The insulin resistance by triglyceride glucose index and risk for
1027 dementia: population-based study. *Alzheimer's Res & Ther* **13,** 1–10.

1028 Huang Z, Thiebaud N and Fadool DA (2017). Differential serotonergic modulation across the main
1029 and accessory olfactory bulbs. *J Physiol* **595,** 3515–3533.

1030 Igarashi KM, Ieki N, An M, Yamaguchi Y, Nagayama S, Kobayakawa K, Kobayakawa R, Tanifuji
1031 M, Sakano H, Chen WR and Mori K (2012). Parallel mitral and tufted cell pathways route
1032 distinct odor information to different targets in the olfactory cortex. *J Neurosci* **32,** 7970–7985.

1033 Jan DD Saint and Westbrook GL (2007). Disynaptic amplification of metabotropic Glutamate
1034 Receptor 1 responses in the olfactory bulb. *J Neurosci* **27,** 132–140.

1035 Jones S, Zylberberg J and Schoppa N (2020). Cellular and synaptic mechanisms that differentiate
1036 mitral cells and superficial tufted cells into parallel output channels in the olfactory bulb. *Front*
1037 *Cell Neurosci* **14,** 443.

1038 Kolling LJ, Tatti R, Lowry T, Loeven AM, Fadool JM and Fadool DA (2022). Modulating the
1039 excitability of olfactory output neurons affects whole-body metabolism. *J Neurosci* **42,** 5966–
1040 5990.

1041 Koni PA, Khanna R, Chang MC, Tang MD, Kaczmarek LK, Schlichter LC and Flavell RA (2003).
1042 Compensatory anion currents in Kv1.3 channel-deficient thymocytes. *J Biol Chem* **278,** 39443–
1043 39451.

1044 Krimer LS and Goldman-Rakic PS (1997). An interface holding chamber for anatomical and
1045 physiological studies of living brain slices. *J Neurosci Meth* **75,** 55–58.

1046 Kuczewski N, Fourcaud-Trocmé N, Savigner A, Thevenet M, Aimé P, Garcia S, Duchamp-Viret P
1047 and Palouzier-Paulignan B (2014). Insulin modulates network activity in olfactory bulb slices:
1048 impact on odour processing. *J Physiol* **592,** 2751–2769.

1049 Kues WA and Wunder F (1992). Heterogeneous expression patterns of mammalian potassium
1050 channel genes in developing and adult rat brain. *Eur J Neurosci* **4,** 1296–1308.

1051 Kuljiš RO and Salković-Petrišić M (2011). Dementia, diabetes, Alzheimer's disease, and insulin
1052 resistance in the brain: progress, dilemmas, new opportunities, and a hypothesis to tackle
1053 intersecting epidemics. *J Alzheimer's Dis* **25,** 29–41.

1054 Kwon Y, Jeon YW, Kwon M, Cho Y, Park D and Shin JE (2020). βPix-d promotes tubulin
1055 acetylation and neurite outgrowth through a PAK/Stathmin1 signaling pathway. *PLoS One* **15,**
1056 e0230814.

1057 Liu A, Savya S and Urban NN (2016). Early odorant exposure increases the number of mitral and
1058 tufted cells associated with a single glomerulus. *J Neurosci* **36,** 11646–11653.

1059 Liu S and Shipley MT (2008). Multiple conductances cooperatively regulate spontaneous bursting in
1060 mouse olfactory bulb external tufted cells. *J Neurosci* **28,** 1625.

1061 Lu S, Das P, Fadool DA and Kaczmarek LK (2010). The slack sodium-activated potassium channel
1062 provides a major outward current in olfactory neurons of Kv1.3-/- super-smeller mice. *J*
1063 *Neurophysiol* **103,** 3311–3319.

1064 Ma J and Lowe G. (2007). Correlated firing in tufted cells of mouse olfactory bulb. *Neurosci*
1065 **169(4),** 1715-1738.

1066 Marks DR and Fadool DA (2007). Post-synaptic density perturbs insulin-induced Kv1.3 channel
1067 modulation via a clustering mechanism involving the SH3 domain. *J Neurochem* **103,** 1608–
1068 1627.

1069 Marks DR, Tucker K, Cavallin MA, Mast TG and Fadool DA (2009). Awake intranasal insulin
1070 delivery modifies protein complexes and alters memory, anxiety, and olfactory behaviors.28. *J*
1071 *Neurosci* **29,** 6734–6751.

1072 Mast TG and Fadool DA (2012). Mature and precursor brain-derived neurotrophic factor have
1073 individual roles in the mouse olfactory bulb. *PLoS ONE* **7,** e31978–e31978.

1074 Mori K (1987). Membrane and synaptic properties of identified neurons in the olfactory bulb. *Prog*
1075 *Neurobiol* **29,** 275–300.

1076 Mori K and Sakano H (2022). Processing of odor information during the respiratory cycle in mice.
1077 *Front Neural Circ* **16,** 861800.

1078 Myers Jr. MG and White MF (1993). The new elements of insulin signaling. Insulin receptor
1079 substrate-1 and proteins with SH2 domains. *Diabetes* **42,** 643–650.

1080 Nagayama S, Enerva A, Fletcher ML, Masurkar A V, Igarashi KM, Mori K and Chen WR (2010).
1081 Differential axonal projection of mitral and tufted cells in the mouse main olfactory system.
1082 *Front Neural Circ* **4,** 120

1083 Nagayama S, Homma R and Imamura F (2014). Neuronal organization of olfactory bulb circuits.
1084 *Front Neural Circuits* **8,** 98.

1085 Najac M, Jan D de Saint, Reguero L, Grandes P and Charpak S (2011). Monosynaptic and
1086 polysynaptic feed-forward inputs to mitral cells from olfactory sensory neurons. *J Neurosci* **31,**
1087 8722–8729.

1088 Nickell WT, Shipley MT and Behbehani MM (1996). Orthodromic synaptic activation of rat
1089 olfactory bulb mitral cells in isolated slices. *Brain Res Bull* **39,** 57–62.

1090 Nikouee A, Khabiri M, Grissmer S and Ettrich R (2012). Charybdotoxin and margatoxin acting on
1091 the human voltage-gated potassium channel h Kv1.3 and its H399N mutant: An experimental
1092 and computational comparison. *J Phys Chem B* **116,** 5132–5140.

1093 Palouzier-Paulignan B, Lacroix MC, Aime P, Baly C, Caillol M, Congar P, Julliard AK, Tucker K
1094 and Fadool DA (2012). Olfaction under metabolic influences. *Chem Senses* **37,** 769–797.

1095 Pinching AJ and Powell TPS (1971a). The neuropil of the periglomerular region of the olfactory
1096 bulb. *J Cell Sci* **9(2),** 379-409.

1097 Pinching AJ and Powell TPS (1971b). The neuron types of the glomerular layer of the olfactory bulb.
1098 *J Cell Sci* **9(2),** 305–345.

1099 Price JL and Powell TP (1970). The mitral and short axon cells of the olfactory bulb. *J Cell Sci* **7,**
1100 631–651.

1101 de Saint Jan D, Hirnet D, Westbrook GL and Charpak S (2009). External Tufted Cells Drive the
1102 Output of Olfactory Bulb Glomeruli. *J Neurosci* **29,** 2043–2052.

1103 Salameh S, Nouel D, Flores C and Hoops D (2017). An optimized immunohistochemistry protocol
1104 for detecting the guidance cue Netrin-1 in neural tissue. *MethodsX* **5,** 1–7.

1105 Saper CB (2009). A guide to the perplexed on the specificity of antibodies. *J Histochem Cytochem*
1106 **57,** 1.

1107 Schoppa NE and Westbrook GL (2001). Glomerulus-specific synchronization of mitral cells in the
1108 olfactory bulb. *Neuron* **31,** 639–651.

1109 Schwartz MW, Figlewicz DP, Baskin DG, Woods SC and Porte Jr. D (1992). Insulin in the brain: a
1110 hormonal regulator of energy balance. *Endocr Rev* **13,** 387–414.

1111 Shepherd GM (2004). *The synaptic organization of the brain*, 5th ed. Shepherd GM. Oxford
1112 University Press.

1113 Spencer VA, Kumar S, Paszkiet B, Fein J and Zmuda JF (2014). Cell culture media for fluorescence
1114 imaging. *Genet Eng Biotechnol News **34,** 10.*

1115 Thiebaud N, Gribble F, Reimann F, Trapp S and Fadool DA (2019). A unique olfactory bulb
1116 microcircuit driven by neurons expressing the precursor to glucagon-like peptide 1. *Scientific*
1117 *Rep* **9,** 15542.

1118 Thiebaud N, Johnson MC, Butler JL, Bell GA, Ferguson KL, Fadool AR, Fadool JC, Gale AM, Gale
1119 DS and Fadool DA (2014). Hyperlipidemic diet causes loss of olfactory sensory neurons,
1120 reduces olfactory discrimination, and disrupts odor-reversal learning. *J Neurosci* **34,** 6970–6984.

1121 Thiebaud N, Llewellyn-Smith IJ, Gribble F, Reimann F, Trapp S and Fadool DA (2016). The incretin
1122 hormone glucagon-like peptide 1 increases mitral cell excitability by decreasing conductance of
1123 a voltage-dependent potassium channel. *J Physiol* **594,** 2607–2628.

1124 Tucker K, Cavallin MA, Jean-Baptiste P, Biju KC, Overton JM, Pedarzani P and Fadool DA (2010).
1125 The Olfactory Bulb: A Metabolic Sensor of Brain Insulin and Glucose Concentrations via a
1126 Voltage-Gated Potassium Channel. *Results Probl Cell Differ* **52,** 147–157.

1127 Tucker K, Cho S, Thiebaud N, Henderson MX and Fadool DA (2013). Glucose sensitivity of mouse
1128 olfactory bulb neurons is conveyed by a voltage-gated potassium channel. *J Physiol* **591,** 2541–
1129 2561.

1130 Tucker K and Fadool DA (2002). Neurotrophin modulation of voltage-gated potassium channels in
1131 rat through TrkB receptors is time and sensory experience dependent. *J Physiol* **542,** 413–429.

1132 Vaaga CE and Westbrook GL (2016). Parallel processing of afferent olfactory sensory information. *J*
1133 *Physiol* **594,** 6715.

1134 Velez P, Schwartz AB, Iyer SR, Warrington A and Fadool DA (2016). Ubiquitin ligase Nedd4-2
1135 modulates Kv1.3 current amplitude and ion channel protein targeting155. *J Neurophysiol* **116,**
1136 671–685.

1137 White MF (1997). The insulin signalling system and the IRS proteins. *Diabetologia* **40 Suppl 2,** S2-
1138 17.

1139 Wickelgren I (1998). Tracking insulin to the mind. *Science (1979)* **280,** 517–519.

1140 Wu S, Zhang Y and De Luca F (2019). The effect of a high-calorie diet on bone growth is mediated
1141 by the insulin receptor. *Bone* 166–175.

1142 Xu J, Koni PA, Wang P, Li G, Kaczmarek L, Wu Y, Li Y, Flavell RA and Desir G V (2003). The
1143 voltage-gated potassium channel Kv1.3 regulates energy homeostasis and body weight. *Human*
1144 *Mol Gen* **12,** 551–559.

1145 Youngstrom IA and Strowbridge BW (2015). Respiratory modulation of spontaneous subthreshold
1146 synaptic activity in olfactory bulb granule cells recorded in awake, head-fixed mice. *J Neurosci*
1147 **35,** 8758.

1148 Zagotta WN and Aldrich RW (1990). Alterations in activation gating of single Shaker A-type
1149 potassium channels by the Sh5 mutation. *J Neurosci* **10,** 1799–1810.

1150 Zhou F-W, Hook C and Puche AC (2023). Frequency-dependent centrifugal modulation of the
1151 activity of different classes of mitral and tufted cells in olfactory bulb. *J Neurophysiol* **129,**
1152 1515–1533.

1153 Zhou Z, Xiong W, Zeng S, Xia A, Shepherd GM, Greer CA and Chen WR (2006). Dendritic
1154 excitability and calcium signaling in the mitral cell distal glomerular tuft. *Eur J Neurosci* **24(6),**
1155 1623-1632.

Zhishang Zhou 1, Wenhui Xiong, Shaoqun Zeng, Andong Xia, Gordon M Shepherd, Charles A Greer, Wei R Chen

Supplemental figures

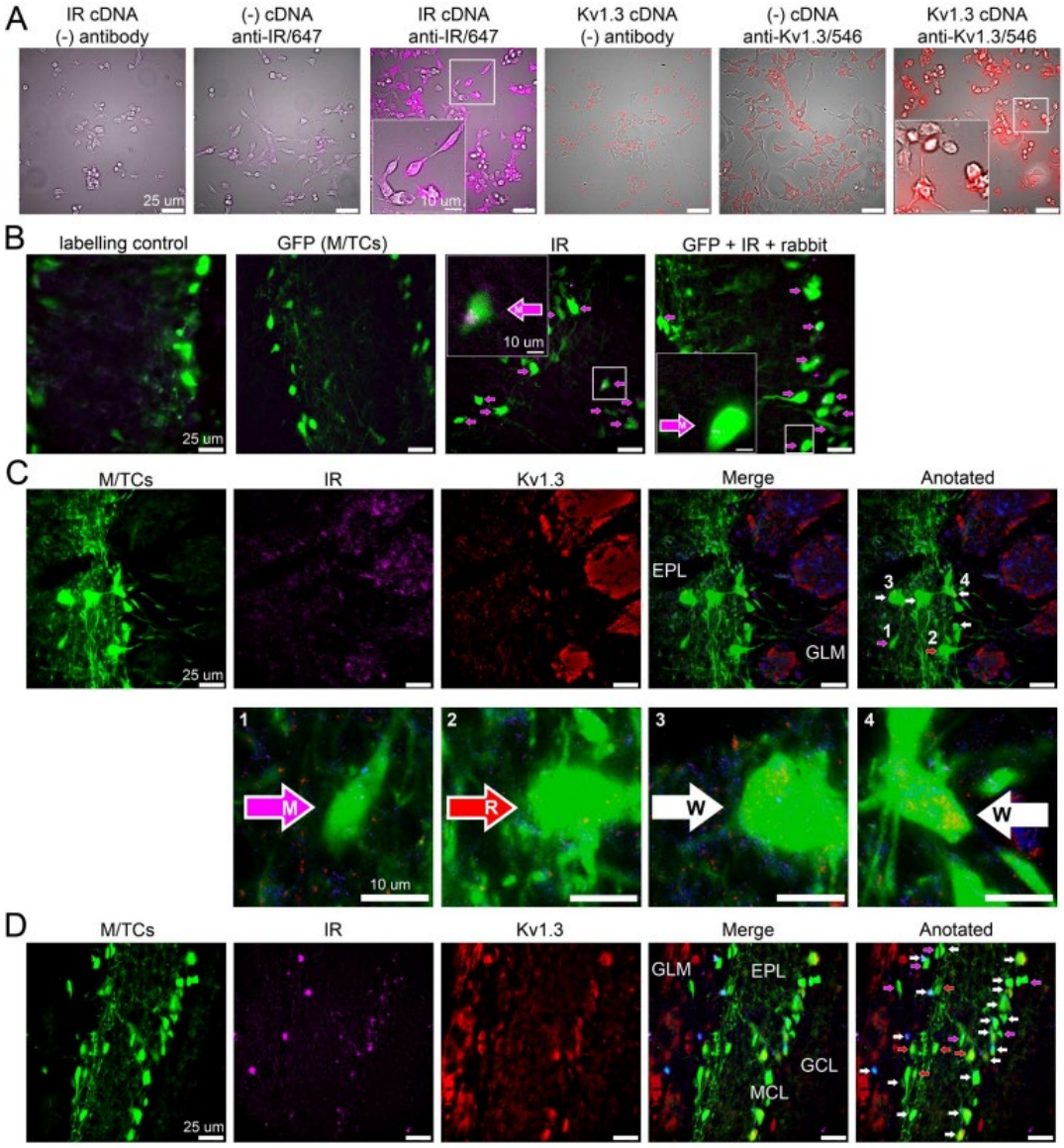

Fig. S1. Colocalization of the insulin receptor (InsR) and Kv1.3 channel (Kv1.3) in superficial tufted cells (sTCs) and mitral cells (MCs). Photomicrographs demonstrating antisera control experiments in ***A,*** HEK 293 cells (*in vitro* specificity controls) and ***B,*** coronal mouse olfactory

1165 bulb sections acquired from GFP mice (*ex vivo* controls where transgenic GFP labels M/TCs
1166 under control of the Tbx21 promoter; green). ***A,*** Cells were transiently transfected with cDNA
1167 encoding the InsR receptor, the Kv1.3 channel, or were mock transfected, and then were
1168 incubated with primary antisera or the omission of primary antisera (***panels 1-6***). ***B,*** Olfactory
1169 bulb sections were incubated with (***panel 1***) omission of primary and secondary antisera,
1170 (***panel 2***) antisera against GFP, (***panel 3***) antiserum against GFP + InsR, or (***panel 4***)
1171 antiserum against GFP + InsR + anti-rabbit. ***C-D,*** Photomicrographs demonstrating labeling
1172 in coronal mouse olfactory bulb sections acquired from GFP mice using both InsR and Kv1.3
1173 antiserum. ***C,*** Separate channels were imaged for endogenous GFP+ M/TCs (***panel 1***), InsR
1174 (***panel 2***), Kv1.3 (***panel 3***), Merge (overlayed green + magenta + red, respectively, yields
1175 cyan; ***panel 4***), and Annotated (see arrow code below, ***panel 5***). ***D,*** Same as in (C), but for
1176 tufted cells and glomeruli (***panel 1***), InsR (***panel 2***), Kv1.3 (***panel 3***), Merge (glomeruli
1177 overlayed magenta + red yields violet; ***panel 4***), and Annotated (***panel 5***).
1178

1179 **Supplemental methods**

1180

1181 **cDNA constructs and antisera**

1182 Insulin receptor (IR) cDNA was a gift from Dr. R. Roth, Stanford University, in the pECE
1183 vector. The entire IR gene was removed using the unique restriction sites Sal I and Xba I, and
1184 ligated into pcDNA3 between the Xho I and Xba I sites in the multiple cloning region under
1185 control of the cytomegalovirus (CMV) promoter (Fadool *et al*., 2000). Rat Kv1.3 (rKv1.3)
1186 was subcloned into the multiple cloning region of $pcDNA_3$ (now available only as 3.1;
1187 RRID:Addgene_23252; originally 3.0 Invitrogen, Carlsbad, CA) at the unique HindIII
1188 restriction site, under control of the CMV promoter (Holmes et al., 1996).
1189

1190 Monoclonal antibodies targeting the beta subunit of the IR or green fluorescent protein were
1191 purchased from Santa Cruz Biotechnology (Dallas, TX, USA). Anti-IR antibody was
1192 purchased pre-conjugated to Alexa Fluor 647 (Anti-INSR catalog # sc-57342 AF647;
1193 RRID:AB_784102); validated by Wu and associates (Wu et al., 2019). Anti-IR antibody was
1194 generated against the C-terminus of the beta subunit of human insulin receptor protein. Anti-
1195 GFP antibody was purchased pre-conjugated to Alexa Fluor 488 (catalog # sc-9996 AF488;

1196 RRID:AB_627695); validated by Kwon and associates (Kwon et al., 2020). Anti-GFP was
1197 generated against amino acids 1-238, representing full length GFP. FSU120, a rabbit
1198 polyclonal antiserum, was generated against the 46-amino acid sequence 478-
1199 MVIEEGGMNHSAFPQTPFKTGNSTATCTTNNNPNDCVNIKKIFTDV-523, representing
1200 the unique coding region of the Kv1.3 channel between transmembrane domain 6 and the
1201 carboxy terminal (Fadool *et al*., 2000). The purified peptide was produced by Genmed
1202 Synthesis (San Francisco, CA, USA), the antiserum was produced and then affinity purified
1203 by Cocalico Biologicals (Reamstown, PA, USA). We have validated this epitope in several
1204 previous studies (Fadool *et al*., 2000, 2004; Colley *et al*., 2007; Marks and Fadool, 2007; Biju
1205 *et al*., 2008; Marks *et al*., 2009) and this latest regeneration of the antisera, specifically (Velez
1206 *et al*., 2016; Kolling *et al*., 2022). Alexa Fluor 546 (Invitrogen, catalog #A-11035;
1207 RRID:AB_2534077) was used to label the FSU120 antibody for imaging.
1208

1209 **Culturing, immunocytochemistry, and immunohistochemistry**

1210 Human embryonic kidney 293 (HEK 293; RRID:CVCL_0045) cells were used that are not
1211 listed as a commonly-misidentified cell line at the International Cell Line Authentication
1212 Committee Registry (ICLACR). Our HEK 293 cells were a generous gift from Dr. Robert
1213 Margolskee (Monell Chemical Senses Center, Philadelphia, PA, USA) and have been
1214 authenticated for cross-contamination and misidentification by profiling the cellular genome.
1215 Cell culture practices at Florida State University have followed "Guidance on Good Cell
1216 Culture Practices" (Coecke et al., 2005). Our most recent cryopreserved batch of HEK 293
1217 cells was prepared in 2016, and each aliquot is used between passages 4 and 25. HEK 293
1218 cells were grown in supplemented Modified Eagle Medium composed of minimal essential
1219 media (MEM; 12360; GIBCO, Life Technologies/ Invitrogen, Durham, NC) plus 2%
1220 penicillin/streptomycin (15140; GIBCO, Invitrogen) and 10% fetal bovine serum (16000;
1221 GIBCO, Invitrogen). Before transient transfection, cells were grown to 90% confluency (7
1222 days), dissociated with trypsin-EDTA (Sigma-Aldrich) and mechanical trituration, diluted in
1223 MEM to a concentration of 600 cells/mL, and replated on Corning dishes (catalog no. 25000;
1224 Thermo Fisher Scientific). To accommodate imaging on a glass substrate, two, 12 mm circle
1225 glass coverslips (Catalog #12-545-90, Thermo Fisher Scientific) were placed flat inside each
1226 35 mm dish. cDNA was introduced into HEK 293 cells with Lipofectamine 3000 transfection

1227 reagent (Invitrogen catalog #L3000015) in OptiMEM serum-reduced media
1228 (Invitrogen/GIBCO) 3-5 days after passage as previously described (Cook and Fadool, 2002).
1229 Briefly, cells were transfected for 4 hours (h) with 1.0 g of each cDNA construct per 35-mm
1230 dish. Plasmid DNA with no coding insert (control vector) served as the control to equalize
1231 total ug of cDNA added to each dish/slip. Thirty-six hours after transfection, cover slips were
1232 placed "cells up" on glass slides and fixed in 4% PFA for 20 min at rt. Cells were rinsed in
1233 two 5-min changes of 1X PBS before proceeding with immunocytochemistry. Cells were first
1234 blocked in blocking buffer for 30 min followed by three 5-min changes of 1X PBS. Antibody
1235 labeling for GFP and IR was performed using a 1:50 dilution in incubation buffer for 60 min
1236 at rt. Labeling for Kv1.3 was performed using a 1:50 dilution in incubation buffer for 90 min
1237 at rt, followed by secondary labeling with a species-specific antibody at a 1:500 dilution in
1238 incubation buffer for 45 min at rt.
1239
1240 Immunohistochemistry (IHC) was performed in the same manner as immunocytochemistry.
1241 GFP mice were anesthetized and then terminated by cardiac perfusion using 4% PFA as
1242 previously described (Thiebaud et al., 2014). The mice were decapitated, and skulls
1243 decalcified to flash freeze the brain in protective medium (Biju *et al*., 2008). Coronal sections
1244 at 14-µm thickness (Model 1850UV, Leica Biosystems) were prepared for slide-mounting.
1245 Labeling control consisted of blocking and incubation in buffer without antibodies. No-
1246 primary (omission of FSU120 primary antisera) and singly-labeled controls were performed to
1247 determine the specificity of the anti-rabbit secondary antibody with pre-conjugated antibodies.
1248 Slides were cover-slipped with Fluoromount-G™ (Invitrogen) before imaging. Imaging was
1249 performed on a Leica confocal microscope (THUNDER Imager, Wetzlar, Germany;
1250 RRID:SCR_023794) using a 40X oil-immersion lens, and appropriate laser lines for each
1251 reporter (475 nm, 551 nm, 642 nm). Post-hoc analyses were performed using Photoshop CS4
1252 (Adobe, San Jose, CA, USA; RRID:SCR_014199). The minimum and maximum thresholds
1253 for each color channel were adjusted uniformly for all images before using the "difference"
1254 feature to align multidimensional images in Photoshop. This method allowed for transient
1255 removal of specific channels in order to more clearly determine co-localization of reporters.
1256